Influence of microstructure on debonding at the fiber/matrix interface in fiber-reinforced polymers under tensile loading

Luca Di Stasio

Division of Materials Science
Department of Engineering Sciences and Mathematics
Luleå University of Technology
Luleå, Sweden

Supervisors:

Janis Varna, Zoubir Ayadi

A mio figlio, Levante Libero Antonio

Abstract

This is an abstract, imported from the file *abstract.tex*.

Contents

Acknowledgments

I bought my first and current car, *La Melanza*, in August 2015, just a few weeks before starting my doctoral studies at Luleå University of Technology and Université de Lorraine. Today, October 2019, the odometer reads kilometers. It has been indeed a long journey, one that has brought me to live in two different countries, France and Sweden, and to visit five more, Germany, Greece, Russia, Italy and Spain, for conferences, summer schools and exchanges. A journey in which I have learned a lot, made new friends and built a family. And, apparently, even managed to write a Ph.D. thesis! No such journey could be ventured alone, and here I would like to thank everyone who helped and supported me in these years.
It is common use to place supervisors at the top of the acknowledgements list, and I will not be any different. However, it is with sincere gratitude that I place them here in the first place. Thus, many thanks to Prof. Janis Varna for accepting me as his Ph.D. student, sharing his knowledge, correcting my mistakes, pointing my efforts in the right direction and always being passionate about research.

Luleå, October 2019
Luca Di Stasio

Part I

Chapter 1

A journey of scales

> ... a “sage”, as an anonymous writer has pointed out, “calls up in the average mind the picture of something grey and pedantic if not green and aromatic”.
>
> Arthur D. Little [2]

1.1 Vision 2030: challenges of the next decade and beyond for the transportation industry

Passion and curiosity should always lie at the heart of the scientific activity, and that ought to be enough to define the value of a research effort. Time is the real arbiter of the significance of a piece of research, as many examples in the history of science show [1][1].However, in these years of increasing mistrust towards scientific research and growing doubts on the value of universities and research institutes, it is worth to reflect on the place of one’s own work.

[1]The Ising-Lenz model is one such example [1]. It was suggested by physicist Wilhelm Lenz to his doctoral student Ernst Ising to study phase transitions in ferromagnetic materials. Ising solved it analytically in 1D as part of his Ph.D. defense in 1925, but the solution for a 1D lattice did not show any phase transition and was thus regarded as a failure. Almost 20 years later, Onsager solved the 2D version of the model and showed the possibility of phase transitions in the Ising-Lenz model. The Ising-Lenz is now widly reknown in the statistical physics community and has been applied in several different fields.

Chapter 2

Modeling damage in FRPC

Chapter 3

The fiber-matrix interface crack problem

References

[1] Stephen G. Brush. "History of the Lenz-Ising Model". In: *Reviews of Modern Physics* 39.4 (Oct. 1967), pp. 883–893. DOI: 10.1103/revmodphys.39.883.

[2] A. D. Little. "The Fifth Estate". In: *Science* 60.1553 (Oct. 1924), pp. 299–306. DOI: 10.1126/science.60.1553.299.

Part II

Paper A

Finite Element solution of the fiber/matrix interface crack problem: convergence properties and mode mixity of the Virtual Crack Closure Technique

Authors:
Luca Di Stasio and Zoubir Ayadi

Reformatted version of paper submitted to:
Finite Elements in Analysis and Design, 2019.

Finite Element solution of the fiber/matrix interface crack problem: convergence properties and mode mixity of the Virtual Crack Closure Technique

Luca Di Stasio[1,2] and Zoubir Ayadi[2]

[1]Luleå University of Technology, University Campus, SE-97187 Luleå, Sweden
[2]Université de Lorraine, EEIGM, IJL, 6 Rue Bastien Lepage, F-54010 Nancy, France

Abstract

The bi-material interface arc crack has been the focus of interest in the composite community, where it is usually referred to as the fiber-matrix interface crack. In this work, we investigate the convergence properties of the Virtual Crack Closure Technique (VCCT) when applied to the evaluation of the Mode I, Mode II and total Energy Release Rate of the fiber-matrix interface crack in the context of the Finite Element Method (FEM). We first propose a synthetic vectorial formulation of the VCCT. Thanks to this formulation, we study the convergence properties of the method, both analytically and numerically. It is found that Mode I and Mode II Energy Release Rate (ERR) possess a logarithmic dependency with respect to the size of the elements in the crack tip neighborhood, while the total ERR is independent of element size.

Keywords: Fiber/matrix interface crack, Bi-material interface arc crack, Linear Elastic Fracture Mechanics (LEFM), Virtual Crack Closure Technique (VCCT), Mode separation, Convergence

1 Introduction

Bi-material interfaces represent the basic load transfer mechanism at the heart of Fiber Reinforced Polymer Composite (FRPC) materials. They are present at the macroscale, in the form of adhesive joints; at the mesoscale, as interfaces between layers with different orientations; at the microscale, as fiber-matrix interfaces. Bi-material interfaces have for long attracted the attention of researchers in Fracture Mechanics [3, 13], due to their hidden complexity.
The problem was first addressed in the 1950's by Williams [31], who derived through a linear elastic asymptotic analysis the stress distribution around an *open* crack (i.e. with crack faces nowhere in contact for any size of the crack) between two infinite half-planes of dissimilar materials. He found the existence of a strong oscillatory behavior in the stress singularity at the crack tip of the form

$$r^{-\frac{1}{2}}\sin\left(\varepsilon\log r\right) \quad \text{with} \quad \varepsilon=\frac{1}{2\pi}\log\left(\frac{1-\beta}{1+\beta}\right), \tag{1}$$

in both Mode I and Mode II. In Eq. 1, β is one of the two parameters introduced by Dundurs [9] to characterize bi-material interfaces:

$$\beta=\frac{\mu_2\left(\kappa_1-1\right)-\mu_1\left(\kappa_2-1\right)}{\mu_2\left(\kappa_1+1\right)+\mu_1\left(\kappa_2+1\right)} \tag{2}$$

where $\kappa=3-4\nu$ in plane strain and $\kappa=\frac{3-4\nu}{1+\nu}$ in plane stress, μ is the shear modulus, ν Poisson's coefficient, and indexes $1,2$ refer to the two bulk materials joined at the interface. Defining a as the length of the crack, it was found that the size of the oscillatory region is in the order of $10^{-6}a$ [12]. Given the oscillatory behaviour of the crack tip singularity of Eq. 1, the definition of Stress Intensity Factor (SIF) $\lim_{r\rightarrow 0}\sqrt{2\pi r}\sigma$ diverges and ceases to be valid [3]. It implies that the Mode mixity problem at the crack tip is ill-posed.
It was furthermore observed, always in the context of Linear Elastic Fracture Mechanics (LEFM), that an interpenetration zone exists close to the crack tip [10, 16] with a length in the order of $10^{-4}a$ [10]. Following conclusions firstly proposed in [16], the presence of a *contact zone* in the crack tip neighborhood, of a length to be determined from the solution of the elastic problem, was introduced in [4] and shown to provide a physically consistent solution to the straight bi-material interface crack problem.
The curved bi-material interface crack, more often refered to as the fiber-matrix interface crack (or debond) due to its relevance in FRPCs, was first treated by England [11] and by Perlman and Sih [20], who provided the analytical solution of stress and displacement fields for a circular inclusion with respectively a single debond and an arbitrary number of debonds. Building on their work, Toya [27] particularized the solution and provided the expression of the Energy Release Rate (ERR) at the crack tip. The same problems exposed previously for the *open* straight bi-material crack were shown to exist also for the *open* fiber-matrix interface crack: the presence of strong oscillations in the crack tip singularity and onset of crack face interpenetration at a critical flaw size.[1]
In order to treat cases more complex than the single partially debonded fiber in an infinite matrix of [11, 20, 27], numerical studies followed. In the 1990's, París and collaborators [18] developed a Boundary Element Method (BEM) with the use of discontinuous singular elements at the crack tip and the Virtual Crack Closure Integral (VCCI) [14] for the evaluation of the Energy Release Rate (ERR). They validated their results [18] with respect to Toya's analytical solution [27] and analyzed the effect of BEM interface discretization on the stress field in the neighborhood of the crack tip [2]. Following Comninou's work on the straight crack [4], they furthermore recognized the importance of contact to retrieve a physical solution avoiding interpenetration [18] and studied the effect of the contact zone on debond ERR [29]. Their algorithm was then applied to investigate the fiber-matrix interface crack under different geometrical configurations and

[1]For the fiber-matrix interface crack, flaw size is measured in terms of the angle $\Delta\theta$ subtended by half of the arc-crack, i.e. $a=2\Delta\theta$.

mechanical loadings [19, 8, 5, 7, 6, 24, 23].
Recently the Finite Element Method (FEM) was also applied to the solution of the fiber-matrix interface crack problem [33, 30, 32], in conjunction with the Virtual Crack Closure Technique (VCCT) [22, 15] for the evaluation of the ERR at the crack tip. In [33], the authors validated their model with respect to the BEM results of [18], but no analysis of the effect of the discretization in the crack tip neighborhood comparable to [2] was proposed. Thanks to the interest in evaluating the ERR of interlaminar delamination, different studies exist in the literature on the effect of mesh discretization on Mode I and Mode II ERR of the bi-material interface crack when evaluated with the VCCT in the context of the FEM [26, 17, 25]. However, no comparable analysis can be found in the literature on mode separation and convergence analysis of the VCCT when applied to the fiber-matrix interface crack (circular bi-material interface crack) problem in the context of a linear elastic FEM solution. In the present article, we first present the FEM formulation of the problem, together with the main geometrical characteristics, material properties, boundary conditions and loading. We then propose a vectorial formulation of the VCCT and express Mode I and Mode II ERR in terms of FEM natural variables. With this tool, we derive an analytical estimate of the ERR convergence and compare it with numerical results.

2 FEM formulation of the fiber-matrix interface crack problem

In order to investigate the fiber-matrix interface crack problem, a 2-dimensional model of a single fiber inserted in a rectangular matrix element is considered (see Figure 1). Total element length and height are respectively $2L$ and L, where L is determined by the fiber radius R_f and the fiber volume fraction V_f by

$$L = \frac{R_f}{2}\sqrt{\frac{\pi}{V_f}}. \tag{3}$$

The fiber radius R_f is assumed to be equal to 1 μm. This choice is not dictated by physical considerations but for simplicity. It is thus useful to remark that, in a linear elastic solution as the one considered in the present work, the ERR is proportional to the geometrical dimensions of the model and, consequently, recalculation of the ERR for fibers of any size requires a simple multiplication.

As shown in Fig. 1, the debond is placed symmetrically with respect to the x axis and its size is characterized by the angle $\Delta\theta$ (which makes the full debond size equal to $2\Delta\theta$ and the full crack length equal to $R_f 2\Delta\theta$). A region $\Delta\Phi$ of unknown size appears at the crack tip for large debond sizes (at least $\geq 60^\circ - 80^\circ$), in which the crack faces are in contact with each other and free to slide. Frictionless contact is thus considered between the two crack faces to allow free sliding and avoid interpenetration. Symmetry with respect to the x axis is applied on the lower boundary while the upper surface is left free. Kinematic coupling on the x-displacement is applied along the left and right

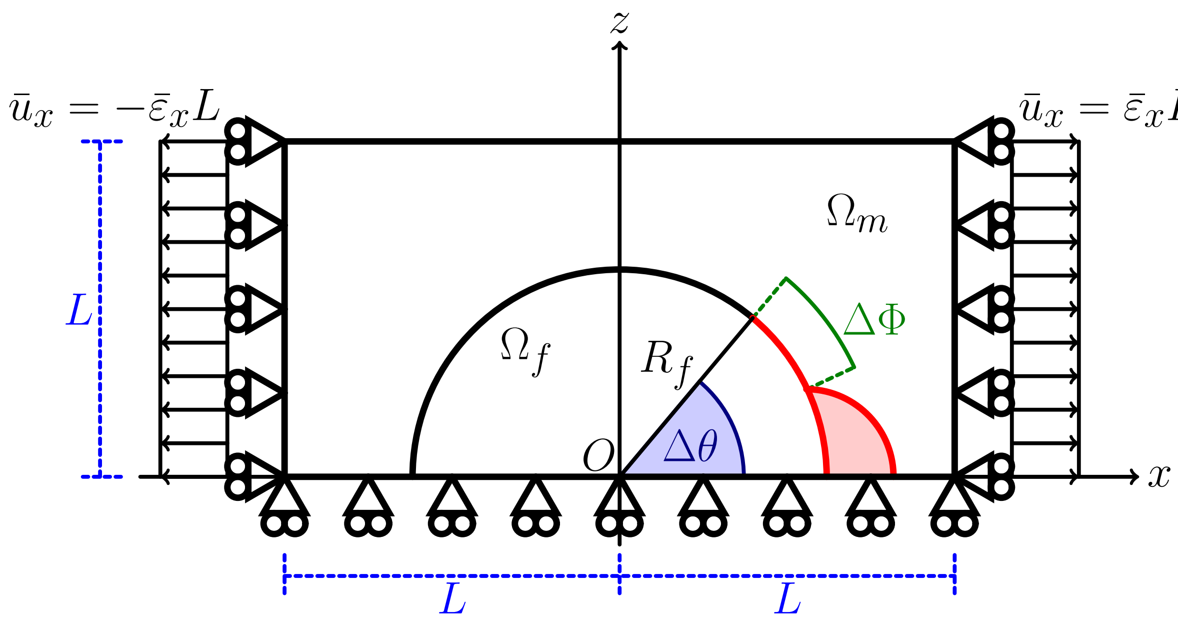

Figure 1: Schematic of the model with its main parameters.

sides of the model in the form of a constant x-displacement $\pm\bar{\varepsilon}_x L$, which corresponds to transverse strain $\bar{\varepsilon}_x$ equal to 1% in the results here presented.

Table 1: Summary of the mechanical properties of fiber and matrix. E stands for Young's modulus, μ for shear modulus and ν for Poisson's ratio.

Material	$E\,[GPa]$	$\mu\,[GPa]$	$\nu\,[-]$
Glass fiber	70.0	29.2	0.2
Epoxy	3.5	1.25	0.4

The model problem is solved with the Finite Element Method (FEM) within the Abaqus environment, a commercial FEM software [1]. The model is meshed with second order, 2D, plane strain triangular (CPE6) and rectangular (CPE8) elements. A regular mesh of rectangular elements with almost unitary aspect ratio is used at the crack tip. The angular size δ of an element in the crack tip neighborhood represents the main parameter of the numerical analysis. The crack faces are modeled as element-based surfaces and a small-sliding contact pair interaction with no friction is imposed between them. The Mode I, Mode II and total Energy Release Rates (ERRs) (respectively referred to as G_I, G_{II} and G_{TOT}) are evaluated using the VCCT [15], implemented in a in-house Python routine. A glass fiber-epoxy system is considered in the present work, and it is assumed that their response lies always in the linear elastic domain. The elastic properties of glass fiber and epoxy are reported in Table 1.

3 Vectorial formulation of the Virtual Crack Closure Technique (VCCT)

In order to express the VCCT formulation of the ERR in terms of FEM variables, we need to introduce a few rotation matrices in order to represent the discretized representation (FE mesh) of a crack along a circular interface. The position of the crack tip is characterized by the angular size of the crack (see Sec. 2 and Fig. 1 for reference) and the rotation corresponding to the crack tip reference frame is represented by the matrix $\underline{\underline{R}}_{\Delta\theta}$ defined as

$$\underline{\underline{R}}_{\Delta\theta} = \begin{bmatrix} \cos(\Delta\theta) & \sin(\Delta\theta) \\ -\sin(\Delta\theta) & \cos(\Delta\theta) \end{bmatrix}. \tag{4}$$

Nodes belonging to the elements sharing the crack tip are involved in the VCCT estimation of the ERR and it is assumed that, given a sufficiently fine discretization, they are aligned with the crack propagation direction defined at the crack tip. However, irrespectively of how small the elements in the crack tip neighborhood are, a misalignment always exists with respect to the assumed crack propagation direction (in the crack tip reference frame). This is measured by the matrices $\underline{\underline{P}}_{\delta}(p)$, defined as

$$\underline{\underline{P}}_{\delta}(p) = \begin{bmatrix} \cos\left(\left(1+\frac{1-p}{m}\right)\delta\right) & \sin\left(\left(1+\frac{1-p}{m}\right)\delta\right) \\ -\sin\left(\left(1+\frac{1-p}{m}\right)\delta\right) & \cos\left(\left(1+\frac{1-p}{m}\right)\delta\right) \end{bmatrix} \tag{5}$$

and $\underline{\underline{Q}}_{\delta}(q)$, equal to

$$\underline{\underline{Q}}_{\delta}(q) = \begin{bmatrix} \cos\left(\frac{q-1}{m}\delta\right) & \sin\left(\frac{q-1}{m}\delta\right) \\ -\sin\left(\frac{q-1}{m}\delta\right) & \cos\left(\frac{q-1}{m}\delta\right) \end{bmatrix}, \tag{6}$$

respectively for the free and bonded nodes involved in the VCCT estimation. In Eqs. 5 and 6, δ is the angular size of an element in the crack tip neighborhood (see Sec. 2 and Fig. 1), m is the order of the element shape functions and p, q are indices referring to the nodes belonging respectively to free and bonded elements sharing the crack tip. Introducing the permutation matrix

$$\underline{\underline{P}}_{\pi} = \begin{bmatrix} 0 & 1 \\ -1 & 0 \end{bmatrix}, \tag{7}$$

it is possible to express the derivatives of rotation matrices $\underline{\underline{R}}_{\Delta\theta}$, $\underline{\underline{P}}_{\delta}$ and $\underline{\underline{Q}}_{\delta}$ with respect to their argument:

$$\frac{\partial \underline{\underline{R}}_{\Delta\theta}}{\partial \Delta\theta} = \underline{\underline{D}} \cdot \underline{\underline{R}}_{\Delta\theta}, \quad \frac{\partial \underline{\underline{P}}_{\delta}}{\partial \delta} = \left(1+\frac{1-p}{m}\right)\underline{\underline{D}} \cdot \underline{\underline{P}}_{\delta}, \quad \frac{\partial \underline{\underline{Q}}_{\delta}}{\partial \delta} = \frac{q-1}{m}\underline{\underline{D}} \cdot \underline{\underline{Q}}_{\delta}. \tag{8}$$

By means of Eqs. 5 and 6, we can express the crack tip forces $\underline{F}_{xy} = \begin{bmatrix} F_x \\ F_y \end{bmatrix}$ and crack displacements $\underline{u}_{xy} = \begin{bmatrix} u_x \\ u_y \end{bmatrix}$ in the crack tip reference frame (where the tangential direction θ correspond to the direction of crack propagation) while taking into account the misalignment to the finite discretization as

$$\underline{F}_{r\theta} = \underline{\underline{Q}}_{\delta}\underline{\underline{R}}_{\Delta\theta}\underline{F}_{xy} \qquad \underline{u}_{r\theta} = \underline{\underline{P}}_{\delta}\underline{\underline{R}}_{\Delta\theta}\underline{u}_{xy} \tag{9}$$

where $\underline{F}_{r\theta} = \begin{bmatrix} F_r \\ F_\theta \end{bmatrix}$ and $\underline{u}_{r\theta} = \begin{bmatrix} u_r \\ u_\theta \end{bmatrix}$.

The crack tip forces can be expressed as a function of the crack opening displacement as

$$\underline{F}_{xy} = \underline{\underline{K}}_{xy}\underline{u}_{xy} + \underline{\widetilde{F}}_{xy}, \tag{10}$$

where $\underline{\underline{K}}_{xy}$ is in general a full matrix of the form $\underline{\underline{K}}_{xy} = \begin{bmatrix} K_{xx} K_{xy} \\ K_{yx} K_{yy} \end{bmatrix}$ and $\underline{\widetilde{F}}_{xy}$ represents the effect of the rest of the FE solution through the remaining nodes of the elements attached to the crack tip. As such, the term $\underline{\widetilde{F}}_{xy}$ can be expressed as a linear combination of the solution vector $\underline{u}_N$ of nodal displacements of the form $\underline{\underline{\widetilde{K}}}_N\underline{u}_N$. Equation 10 thus become

$$\underline{F}_{xy} = \underline{\underline{K}}_{xy}\underline{u}_{xy} + \underline{\underline{\widetilde{K}}}_N\underline{u}_N. \tag{11}$$

An exemplifying derivation of the relationships expressed in Equations 10 and 11 can be found in A. It is worthwhile to observe that another author [28] proposed a relationship of the form $\underline{F}_{xy} = \underline{\underline{K}}_{xy}\underline{u}_{xy}$. However, in [28], this relationship is assumed *a priori* and manipulated to propose a revised version of the VCCT, based on the assumption that the matrix $\underline{\underline{K}}_{xy}$ should be diagonal to provide physically-consistent fracture mode partitioning. On the other hand, in the present work we derive the relationships of Eqs. 10 and 11 from the formulation of the Finite Element Method. According to our derivation, it seems correct that the matrix $\underline{\underline{K}}_{xy}$ should not in general be diagonal in order to take into account Poisson's effect. In fact, a positive crack opening displacement would cause a transverse displacement in the neighborhood of the crack tip. Given that material properties are different on the two sides of a bi-material interface, a net shear would be applied to the crack tip which would correspond to a net contribution to the crack tip force related to crack shear displacement. The analytical derivations presented in A confirm these physical considerations.

Based upon the work of Raju [21], we introduce the matrix $\underline{\underline{T}}_{pq}$ to represent the weights needed in the VCCT to account for the use of singular elements. As already done previously, indices p and q refer to nodes placed respectively on the free (crack face) and bonded side of the crack tip. Nodes are enumerated so that the crack tip has always index 1, i.e. the higher the index the further the node is from the crack tip. Matrix $\underline{\underline{T}}_{pq}$ has always a size of $d \times d$, where $d = 2$ for a $2D$ problem and $d = 3$ for a $3D$ problem. An element $\underline{\underline{T}}_{pq}(i, j)$ with $i, j = 1, \ldots, d$ represents the weight to be assigned to the product of component i of the displacement extracted at node p with component j of the force extracted at node q. The expression of for quadrilateral elements with or

without singularity is reported in B. Notice that, given m is the order of the element shape functions, the element side has $m+1$ nodes and this represents the upper limit of indices p and q.
By using matrix $\underline{\underline{T}}_{pq}$, it is possible to express the total ERR G evaluated with the VCCT as

$$G_{TOT} = \frac{1}{2R_f\delta}\sum_{p=1}^{m+1}\sum_{q=1}^{m+1} Tr\left(\underline{u}_{r\theta,p}^T \underline{\underline{T}}_{pq}^T \underline{F}_{r\theta,q}\right). \tag{12}$$

Introducing the vector $\underline{G} = \begin{bmatrix} G_I \\ G_{II} \end{bmatrix}$ of fracture mode ERRs, Mode I and Mode II ERR evaluated with the VCCT can be expressed as

$$\underline{G} = \frac{1}{2R_f\delta}\sum_{p=1}^{m+1}\sum_{q=1}^{m+1} Diag\left(\underline{F}_{r\theta,q}\underline{u}_{r\theta,p}^T \underline{\underline{T}}_{pq}^T\right), \tag{13}$$

where $Diag\,()$ is the function that extracts the main diagonal of the input matrix as a column vector. Substituting Equations 9 and 11 in Equations 12 and 13, we can express the Mode I, Mode II and total Energy Release Rate as a function of the crack displacements and the FE solution (more details in A) as

$$\begin{aligned} G_{TOT} =& \frac{1}{2R_f\delta}\sum_{p=1}^{m+1}\sum_{q=1}^{m+1} Tr\left(\underline{\underline{Q}}_{\delta}\underline{\underline{R}}_{\Delta\theta}\underline{\underline{K}}_{xy,q}\underline{u}_{xy,q}\underline{u}_{xy,p}^T\underline{\underline{R}}_{\Delta\theta}^T\underline{\underline{P}}_{\delta}^T\underline{\underline{T}}_{pq}^T\right) + \\ &+ \frac{1}{2R_f\delta}\sum_{p=1}^{m+1}\sum_{q=1}^{m+1} Tr\left(\underline{\underline{Q}}_{\delta}\underline{\underline{R}}_{\Delta\theta}\underline{\widetilde{F}}_{xy,q}\underline{u}_{xy,p}^T\underline{\underline{R}}_{\Delta\theta}^T\underline{\underline{P}}_{\delta}^T\underline{\underline{T}}_{pq}^T\right) \end{aligned} \tag{14}$$

and

$$\begin{aligned} \underline{G} = \begin{bmatrix} G_I \\ G_{II} \end{bmatrix} =& \frac{1}{2R_f\delta}\sum_{p=1}^{m+1}\sum_{q=1}^{m+1} Diag\left(\underline{\underline{Q}}_{\delta}\underline{\underline{R}}_{\Delta\theta}\underline{\underline{K}}_{xy,q}\underline{u}_{xy,q}\underline{u}_{xy,p}^T\underline{\underline{R}}_{\Delta\theta}^T\underline{\underline{P}}_{\delta}^T\underline{\underline{T}}_{pq}^T\right) + \\ &+ \frac{1}{2R_f\delta}\sum_{p=1}^{m+1}\sum_{q=1}^{m+1} Diag\left(\underline{\underline{Q}}_{\delta}\underline{\underline{R}}_{\Delta\theta}\underline{\underline{\widetilde{K}}}_{N,q}\underline{u}_{N}\underline{u}_{xy,p}^T\underline{\underline{R}}_{\Delta\theta}^T\underline{\underline{P}}_{\delta}^T\underline{\underline{T}}_{pq}^T\right) \end{aligned} \tag{15}$$

4 Rotational invariance of G_{TOT}

Recalling Equation 14 and observing that matrix $\underline{\underline{T}}_{pq}$ is always equal to the identity matrix pre-multiplied by a suitable real constant (see Eq. B.52 in B), the total Energy Release Rate can be rewritten as

$$
\begin{aligned}
G_{TOT} &= \frac{1}{2R_f\delta}\sum_{p=1}^{m+1}\sum_{q=1}^{m+1} Tr\left(\underline{\underline{Q}}_{\delta}\underline{\underline{R}}_{\Delta\theta}\left(\underline{\underline{K}}_{xy,q}\underline{u}_{xy,q}+\underline{\widetilde{F}}_{xy,q}\right)\underline{u}^{T}_{xy,p}\underline{\underline{T}}^{T}_{pq}\underline{\underline{R}}^{T}_{\Delta\theta}\underline{\underline{P}}^{T}_{\delta}\right) = \\
&= \frac{1}{2R_f\delta}\sum_{p=1}^{m+1}\sum_{q=1}^{m+1} Tr\left(\underline{\underline{Q}}_{\delta}\underline{\underline{R}}_{\Delta\theta}\underline{F}_{xy,q}\underline{u}^{T}_{xy,p}\underline{\underline{T}}^{T}_{pq}\underline{\underline{R}}^{T}_{\Delta\theta}\underline{\underline{P}}^{T}_{\delta}\right),
\end{aligned}
\tag{16}
$$

where $\underline{F}_{xy}$ and $\underline{u}_{xy}$ are the vectors of respectively the crack tip forces and crack displacements in the global $(x-y)$ reference frame. Given that $\underline{\underline{Q}}_{\delta}$, $\underline{\underline{P}}_{\delta}$ and $\underline{\underline{R}}_{\Delta\theta}$ all represent a linear transformation (a rigid rotation in particular), the invariance of the trace to linear transformations ensures that

$$
\begin{aligned}
G_{TOT} &= \frac{1}{2R_f\delta}\sum_{p=1}^{m+1}\sum_{q=1}^{m+1} Tr\left(\underline{\underline{Q}}_{\delta}\underline{\underline{R}}_{\Delta\theta}\underline{F}_{xy,q}\underline{u}^{T}_{xy,p}\underline{\underline{T}}^{T}_{pq}\underline{\underline{R}}^{T}_{\Delta\theta}\underline{\underline{P}}^{T}_{\delta}\right) = \\
&= \frac{1}{2R_f\delta}\sum_{p=1}^{m+1}\sum_{q=1}^{m+1} Tr\left(\underline{F}_{xy,q}\underline{u}^{T}_{xy,p}\underline{\underline{T}}^{T}_{pq}\right).
\end{aligned}
\tag{17}
$$

As G_{TOT} was defined according to Equation 12 and given that $Tr\left(AB\right) = Tr\left(BA\right)$, it holds that

$$
\begin{aligned}
G_{TOT} &= \frac{1}{2R_f\delta}\sum_{p=1}^{m+1}\sum_{q=1}^{m+1} \underline{u}^{T}_{r\theta,p}\underline{\underline{T}}^{T}_{pq}\underline{F}_{r\theta,q} = \frac{1}{2R_f\delta}\sum_{p=1}^{m+1}\sum_{q=1}^{m+1} Tr\left(\underline{F}_{r\theta,q}\underline{u}^{T}_{r\theta,p}\underline{\underline{T}}^{T}_{pq}\right) = \\
&= \frac{1}{2R_f\delta}\sum_{p=1}^{m+1}\sum_{q=1}^{m+1} Tr\left(\underline{F}_{xy,q}\underline{u}^{T}_{xy,p}\underline{\underline{T}}^{T}_{pq}\right) = \frac{1}{2R_f\delta}\sum_{p=1}^{m+1}\sum_{q=1}^{m+1} \underline{u}^{T}_{xy,p}\underline{\underline{T}}^{T}_{pq}\underline{F}_{xy,q}
\end{aligned}
\tag{18}
$$

which shows that the total Energy Release Rate is invariant to rigid rotations and can be calculated equivalently with forces and displacements expressed in the local crack tip reference frame or the global reference frame. The analytical result is confirmed by the numerical solution of the fiber-matrix interface crack with different element orders and model fiber volume fractions, as shown in Figure 2.

The result of Equation 18 has also physical implications:

– given that stress and displacement fields at the crack tip are the same, two cracks with different crack paths are energetically equivalent with respect to the total Energy Release Rate;

– given that laws of the type $G_{TOT} \geq G_c$ govern crack propagation, if G_c do not depend on mode ratio, crack orientation will not affect its growth.

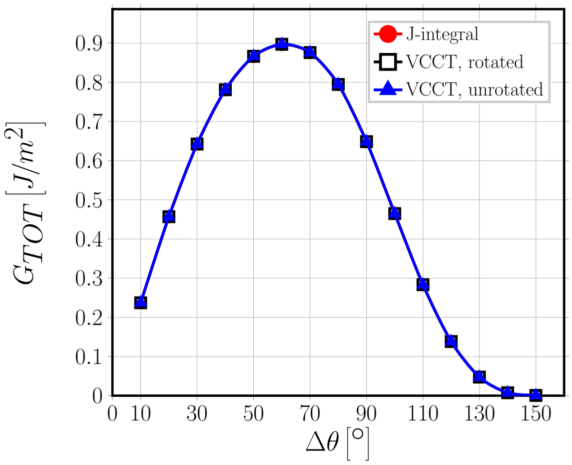

(a) $V_f = 0.1\%$, 1^{st} order elements, $\delta = 0.05°$.

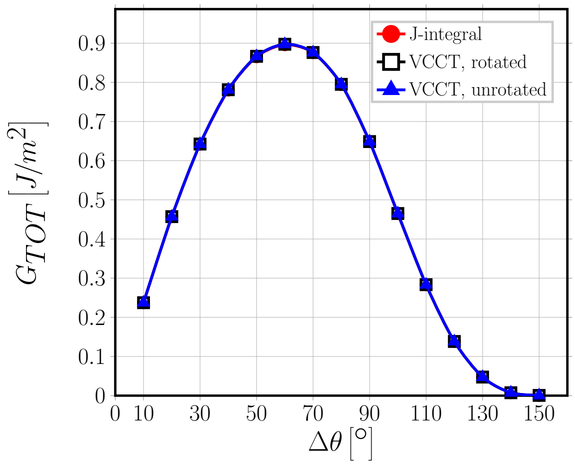

(b) $V_f = 0.1\%$, 2^{nd} order elements, $\delta = 0.05°$.

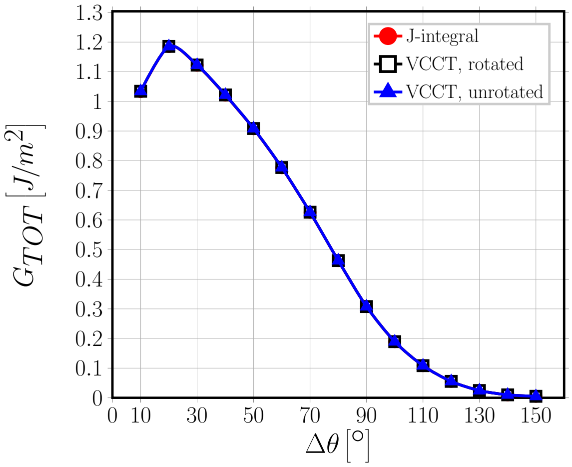

(c) $V_f = 40\%$, 1^{st} order elements, $\delta = 0.05°$.

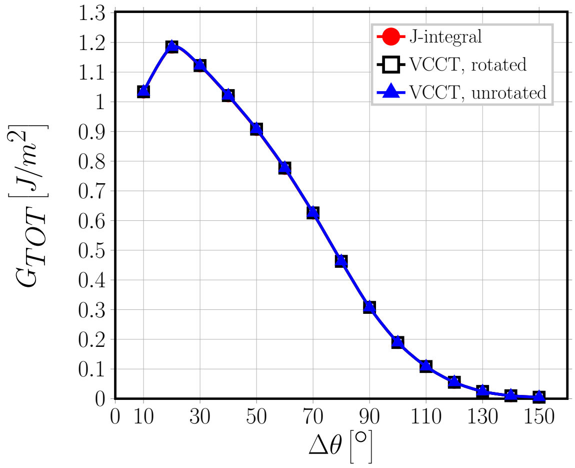

(d) $V_f = 40\%$, 2^{nd} order elements, $\delta = 0.05°$.

Figure 2: Numerical invariance of the total Energy Release Rate: G_{TOT} computed with the VCCT with rotated forces and displacements (label rotated*), with the VCCT with forces and displacements in the global reference frame (label* unrotated*) and with J-integral method (label* J-integral*).*

5 Convergence analysis

5.1 Analytical considerations

Substituting Equations 8 in the derivative of Equation 13, we can investigate the dependency of Mode I and Mode II ERR with respect to the size δ of an element in the crack tip neighborhood through

$$
\begin{aligned}
\frac{\partial \underline{G}}{\partial \delta} =& -\frac{1}{2R_f\delta^2}\sum_{p=1}^{m+1}\sum_{q=1}^{m+1} Diag\left(\underline{\underline{Q}}_{\delta}\underline{\underline{R}}_{\Delta\theta}\underline{\underline{K}}_{xy}\underline{u}_{xy}\underline{u}_{xy}^{T}\underline{\underline{R}}_{\Delta\theta}^{T}\underline{\underline{P}}_{\delta}^{T}\underline{\underline{T}}_{pq}^{T}\right) - \frac{1}{2R_f\delta^2}\sum_{p=1}^{m+1}\sum_{q=1}^{m+1} Diag\left(\underline{\underline{Q}}_{\delta}\underline{\underline{R}}_{\Delta\theta}\underline{\underline{\widetilde{K}}}_{N}\underline{u}_{N}\underline{u}_{xy}^{T}\underline{\underline{R}}_{\Delta\theta}^{T}\underline{\underline{P}}_{\delta}^{T}\underline{\underline{T}}_{pq}^{T}\right) + \\
&+\frac{1}{2R_f\delta}\sum_{p=1}^{m+1}\sum_{q=1}^{m+1} Diag\left(\underline{\underline{Q}}_{\delta}\underline{\underline{R}}_{\Delta\theta}\underline{\underline{K}}_{xy}\underline{u}_{xy}\underline{u}_{xy}^{T}\underline{\underline{R}}_{\Delta\theta}^{T}\underline{\underline{P}}_{\delta}^{T}\underline{\underline{D}}^{T}\underline{\underline{T}}_{pq}^{T}\right) + \frac{1}{2R_f\delta}\sum_{p=1}^{m+1}\sum_{q=1}^{m+1} Diag\left(\underline{\underline{Q}}_{\delta}\underline{\underline{R}}_{\Delta\theta}\underline{\underline{\widetilde{K}}}_{N}\underline{u}_{N}\underline{u}_{xy}^{T}\underline{\underline{R}}_{\Delta\theta}^{T}\underline{\underline{P}}_{\delta}^{T}\underline{\underline{D}}^{T}\underline{\underline{T}}_{pq}^{T}\right) + \\
&+\frac{1}{2R_f\delta}\sum_{p=1}^{m+1}\sum_{q=1}^{m+1} Diag\left(\underline{\underline{D}}\underline{\underline{Q}}_{\delta}\underline{\underline{R}}_{\Delta\theta}\underline{\underline{K}}_{xy}\underline{u}_{xy}\underline{u}_{xy}^{T}\underline{\underline{R}}_{\Delta\theta}^{T}\underline{\underline{P}}_{\delta}^{T}\underline{\underline{T}}_{pq}^{T}\right) + \frac{1}{2R_f\delta}\sum_{p=1}^{m+1}\sum_{q=1}^{m+1} Diag\left(\underline{\underline{D}}\underline{\underline{Q}}_{\delta}\underline{\underline{R}}_{\Delta\theta}\underline{\underline{\widetilde{K}}}_{N}\underline{u}_{N}\underline{u}_{xy}^{T}\underline{\underline{R}}_{\Delta\theta}^{T}\underline{\underline{P}}_{\delta}^{T}\underline{\underline{T}}_{pq}^{T}\right) + \\
&+\frac{1}{2R_f\delta}\sum_{p=1}^{m+1}\sum_{q=1}^{m+1} Diag\left(\underline{\underline{Q}}_{\delta}\underline{\underline{R}}_{\Delta\theta}\underline{\underline{K}}_{xy}\frac{\partial \underline{u}_{xy}}{\partial \delta}\underline{u}_{xy}^{T}\underline{\underline{R}}_{\Delta\theta}^{T}\underline{\underline{P}}_{\delta}^{T}\underline{\underline{T}}_{pq}^{T}\right) + \frac{1}{2R_f\delta}\sum_{p=1}^{m+1}\sum_{q=1}^{m+1} Diag\left(\underline{\underline{Q}}_{\delta}\underline{\underline{R}}_{\Delta\theta}\underline{\underline{\widetilde{K}}}_{N}\frac{\partial \underline{u}_{N}}{\partial \delta}\underline{u}_{xy}^{T}\underline{\underline{R}}_{\Delta\theta}^{T}\underline{\underline{P}}_{\delta}^{T}\underline{\underline{T}}_{pq}^{T}\right) + \\
&+\frac{1}{2R_f\delta}\sum_{p=1}^{m+1}\sum_{q=1}^{m+1} Diag\left(\underline{\underline{Q}}_{\delta}\underline{\underline{R}}_{\Delta\theta}\underline{\underline{K}}_{xy}\underline{u}_{xy}\frac{\partial \underline{u}_{xy}^{T}}{\partial \delta}\underline{\underline{R}}_{\Delta\theta}^{T}\underline{\underline{P}}_{\delta}^{T}\underline{\underline{T}}_{pq}^{T}\right) + \frac{1}{2R_f\delta}\sum_{p=1}^{m+1}\sum_{q=1}^{m+1} Diag\left(\underline{\underline{Q}}_{\delta}\underline{\underline{R}}_{\Delta\theta}\underline{\underline{\widetilde{K}}}_{N}\underline{u}_{N}\frac{\partial \underline{u}_{xy}^{T}}{\partial \delta}\underline{\underline{R}}_{\Delta\theta}^{T}\underline{\underline{P}}_{\delta}^{T}\underline{\underline{T}}_{pq}^{T}\right);
\end{aligned}
\tag{19}
$$

which, after refactoring, provides

$$
\begin{aligned}
\frac{\partial \underline{G}}{\partial \delta} =& \frac{1}{\delta}\underline{G} + \frac{1}{2R_f\delta}\sum_{p=1}^{m+1}\sum_{q=1}^{m+1} Diag\left(\underline{\underline{Q}}_{\delta}\underline{\underline{R}}_{\Delta\theta}\left(\underline{\underline{K}}_{xy}\underline{u}_{xy} + \underline{\underline{\widetilde{K}}}_{N}\underline{u}_{N}\right)\underline{u}_{xy}^{T}\underline{\underline{R}}_{\Delta\theta}^{T}\underline{\underline{P}}_{\delta}^{T}\underline{\underline{D}}^{T}\underline{\underline{T}}_{pq}^{T}\right) + \\
&+\frac{1}{2R_f\delta}\sum_{p=1}^{m+1}\sum_{q=1}^{m+1} Diag\left(\underline{\underline{D}}\underline{\underline{Q}}_{\delta}\underline{\underline{R}}_{\Delta\theta}\left(\underline{\underline{K}}_{xy}\underline{u}_{xy} + \underline{\underline{\widetilde{K}}}_{N}\underline{u}_{N}\right)\underline{u}_{xy}^{T}\underline{\underline{R}}_{\Delta\theta}^{T}\underline{\underline{P}}_{\delta}^{T}\underline{\underline{T}}_{pq}^{T}\right) + \\
&+\frac{1}{R_f\delta}\sum_{p=1}^{m+1}\sum_{q=1}^{m+1} Diag\left(\underline{\underline{Q}}_{\delta}\underline{\underline{R}}_{\Delta\theta}\underline{\underline{K}}_{xy}\frac{\partial \underline{u}_{xy}}{\partial \delta}\underline{u}_{xy}^{T}\underline{\underline{R}}_{\Delta\theta}^{T}\underline{\underline{P}}_{\delta}^{T}\underline{\underline{T}}_{pq}^{T}\right) + \frac{1}{2R_f\delta}\sum_{p=1}^{m+1}\sum_{q=1}^{m+1} Diag\left(\underline{\underline{Q}}_{\delta}\underline{\underline{R}}_{\Delta\theta}\underline{\underline{\widetilde{K}}}_{N}\frac{\partial \underline{u}_{N}}{\partial \delta}\underline{u}_{xy}^{T}\underline{\underline{R}}_{\Delta\theta}^{T}\underline{\underline{P}}_{\delta}^{T}\underline{\underline{T}}_{pq}^{T}\right) + \\
&+\frac{1}{2R_f\delta}\sum_{p=1}^{m+1}\sum_{q=1}^{m+1} Diag\left(\underline{\underline{Q}}_{\delta}\underline{\underline{R}}_{\Delta\theta}\underline{\underline{\widetilde{K}}}_{N}\underline{u}_{N}\frac{\partial \underline{u}_{xy}^{T}}{\partial \delta}\underline{\underline{R}}_{\Delta\theta}^{T}\underline{\underline{P}}_{\delta}^{T}\underline{\underline{T}}_{pq}^{T}\right).
\end{aligned}
\tag{20}
$$

Following the asymptotic analysis of [31, 3], in the case of an *open crack* the displacement in the crack tip neighborhood will have a functional form of the type

$$
u\left(\delta\right) \sim \sqrt{\delta}\left(\sin, \cos\right)\left(\epsilon \log \delta\right) \quad \text{with} \quad \epsilon = \frac{1}{2\pi}\log\left(\frac{1-\beta}{1+\beta}\right) \tag{21}
$$

and β is Dundurs' parameter introduced in Section 1. Application of Equation 21 to the terms on the right hand side of Eq. 20 provides:

$$
\underline{u}_{xy}, \underline{u}_{N} \sim u\left(\delta\right) \sim \sqrt{\delta}\left(\sin, \cos\right)\left(\epsilon \log \delta\right) \xrightarrow{\delta \to 0} 0; \tag{22}
$$

$$
\underline{u}_{xy}\underline{u}_{xy}^{T}, \underline{u}_{N}\underline{u}_{xy}^{T} \sim u^{2}\left(\delta\right) \sim \delta\left(\sin^{2}, \cos^{2}, \sin\cdot\cos\right)\left(\epsilon \log \delta\right) \xrightarrow{\delta \to 0} 0; \tag{23}
$$

$$
\frac{\partial \underline{u}_{xy}}{\partial \delta}\underline{u}_{xy}^{T}, \frac{\partial \underline{u}_{N}}{\partial \delta}\underline{u}_{xy}^{T} \sim -\frac{1}{2}\left(\sin^{2}, \cos^{2}, \sin\cdot\cos\right)\left(\epsilon \log \delta\right) + \left(-\sin^{2}, \cos^{2}, \pm\sin\cdot\cos\right)\left(\epsilon \log \delta\right) \xrightarrow{\delta \to 0} finite; \tag{24}
$$

$$\underline{G} \sim \frac{1}{\delta}\underline{u}_{xy}\underline{u}_{xy}^{T} \sim \frac{1}{\delta}u^{2}\left(\delta\right) \sim \left(\sin^{2}, \cos^{2}, \sin\cdot\cos\right)\left(\epsilon\log\delta\right) \xrightarrow{\delta\to 0} finite. \tag{25}$$

In Equations 22-25, the multiplication by a trigonometric function of the type $\left(\sin, \cos, \sin^2, \cos^2, \mathrm{s}\right.$ prevents the divergence of the asymptote. Recalling Eqs. 5 and 6, in the limit of $\delta \to 0$ the rotation matrices become equal to the identity matrix:

$$\underline{\underline{P}}_{\delta}, \underline{\underline{Q}}_{\delta} \xrightarrow{\delta\to 0} \begin{bmatrix} 1 & 0 \\ 0 & 1 \end{bmatrix}. \tag{26}$$

Applying the results of Equations 22-26 to Eq. 20, it can be shown that the derivative of $\underline{G}$ can be split in a factor that goes to 0 in the limit of $\delta \to 0$ and in a factor independent of δ:

$$\lim_{\delta\to 0}\frac{\partial\underline{G}}{\partial\delta} \sim \frac{1}{\delta}\left(\cancelto{0}{\underline{F}(\delta)} + \underline{C}\right). \tag{27}$$

Thus, asymptotically, the Mode I and Mode II Energy Release Rate behave like the logarithm of the angular size δ of the elements in the crack tip neighborhood:

$$\lim_{\delta\to 0}\frac{\partial\underline{G}}{\partial\delta} \sim \frac{1}{\delta} \quad \xrightarrow{\int d\delta} \quad \lim_{\delta\to 0}\underline{G} \sim \underline{A}\log(\delta) + \underline{B}. \tag{28}$$

5.2 Numerical results

Evaluations of the Mode I, Mode II and total Energy Release Rate using the VCCT applied to the FE solution of the fiber-matrix interface crack in the single fiber model of Sec. 2 are reported respectively in Fig. 3, Fig. 4 and Fig. 5.

Results for Mode I ERR in Fig. 3 show clearly the transition from the *open* crack regime, where Mode I ERR is different from zero, to the *closed* crack regime of the debond, where $G_I = 0$. Looking at Fig. 3, the crack is *open* for $\Delta\theta \leq 60°$ and it is *closed*, i.e. a contact zone is present, for $\Delta\theta \geq 70°$. As expected from the analysis of the previous section, and given that Mode I ERR is different from zero only in the *open* crack regime, a significant dependence on the element size δ can be observed in Fig. 3 when using both 1^{st} and 2^{nd} order elements and with both an effectively infinite ($V_f = 0.1\%$) and finite size ($V_f = 40\%$) matrix. At first sight, it is immediate to see from Fig. 3 that a decrease in δ leads to a decrease in G_I. However, two further effects can be observed due to the refinement of the mesh at the crack tip, i.e. the decrease of the element size δ. First, the occurrence of the peak G_I is shifted to lower angles for very low volume fractions: it occurs at $\Delta\theta = 30°$ with $\delta = 1.0°, 0.5°$ and at $\Delta\theta = 20°$ with $\delta \leq 0.25°$ for both 1^{st} and 2^{nd} order elements and $V_f = 0.1\%$. Second, the apperance of the contact zone, i.e. the switch to the *closed* crack regime, is anticipated to smaller debonds: it occurs at $\Delta\theta = 70°$ with $\delta \geq 0.2°$ and at $\Delta\theta = 60°$ with $\delta < 0.2°$ for both 1^{st} and 2^{nd} order elements and both $V_f = 0.1\%$ and $V_f = 40\%$.

Observing Figure 4, it possible to notice the existence of two distinct regimes in the behavior of G_{II} with respect to the element size δ. For $\Delta\theta \leq 60°$ G_{II} depends on the

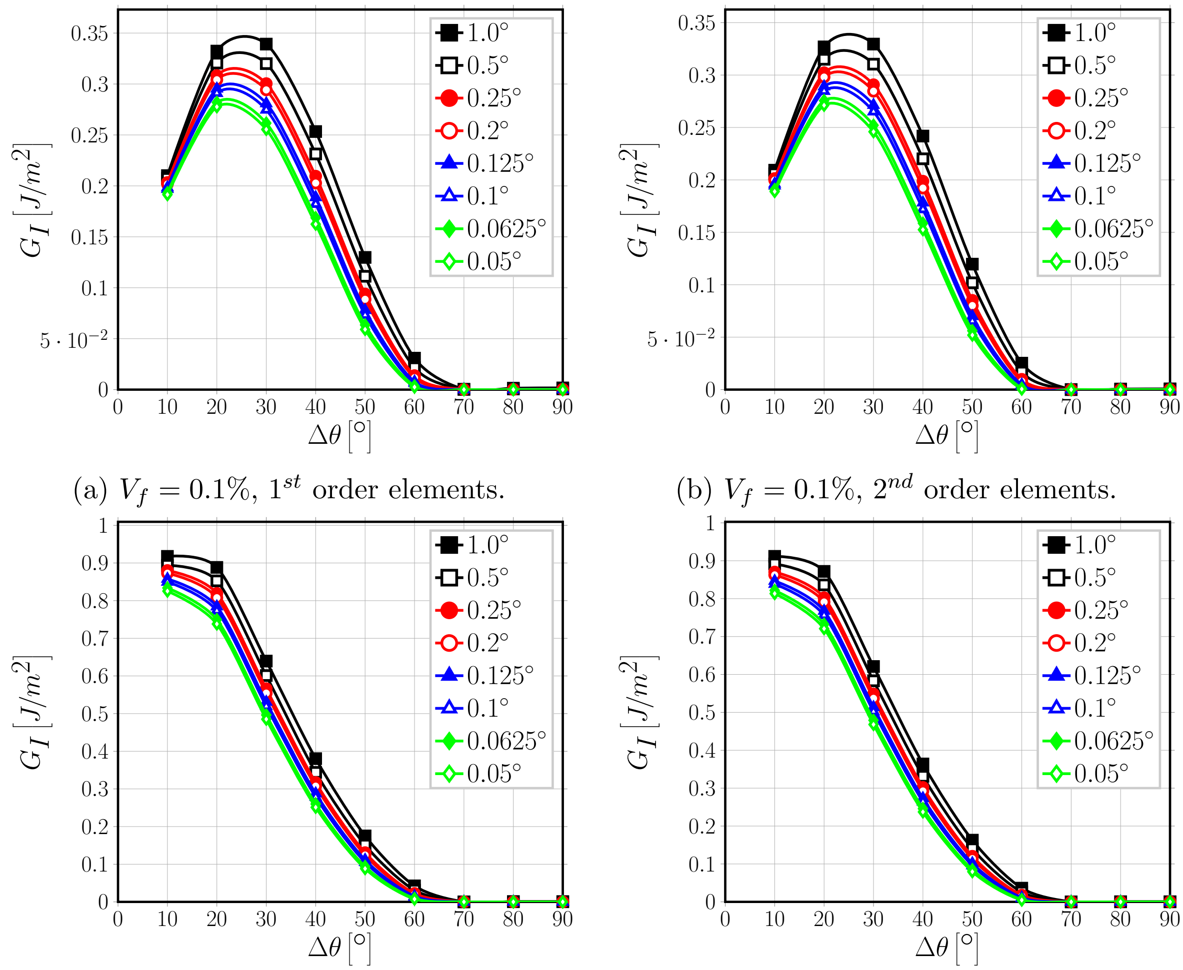

(a) $V_f = 0.1\%$, 1^{st} order elements.

(b) $V_f = 0.1\%$, 2^{nd} order elements.

(c) $V_f = 40\%$, 1^{st} order elements.

(d) $V_f = 40\%$, 2^{nd} order elements.

Figure 3: Effect of the size δ of an element at the crack tip on Mode I ERR.

value of δ, while $\Delta\theta \geq 70°$ it is effectively independent of the element size at the crack tip for both 1^{st} and 2^{nd} order elements and both an effectively infinite ($V_f = 0.1\%$) and finite size ($V_f = 40\%$) matrix. Comparing the value of $\Delta\theta$ at which the change from the δ-dependency regime to the δ-independency regime occurs for G_{II} with Mode I ERR in Fig. 3, it is possible to observe that the δ-dependency regime change of Mode II ERR coincides with the onset of the contact zone, i.e. the transition from *open* crack regime to the *closed* crack regime. The result confirms the analytical considerations of the previous section: for an *open* crack both Mode I and Mode II ERR depend on the element size δ at the crack tip.

Further observation of Figure 4 reveals that, in the *open* crack regime, decreasing the element size δ causes an increase of Mode II ERR. Similarly to Mode I ERR, a shift of the peak G_{II} can also observed for $V_f = 0.1\%$: the maximum value of G_{II} occurs at $\Delta\theta = 70°$ for $\delta > 0.25°$ for 1^{st} order elements and for $\delta > 0.5°$ for 2^{nd} order elements, while it is shifted to $\Delta\theta = 60°$ for $\delta \leq 0.25°$ for 1^{st} order elements and for $\delta \leq 0.5°$ for

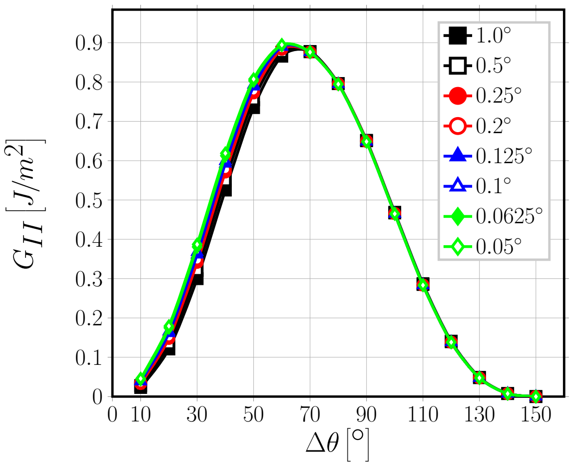

(a) $V_f = 0.1\%$, 1^{st} order elements.

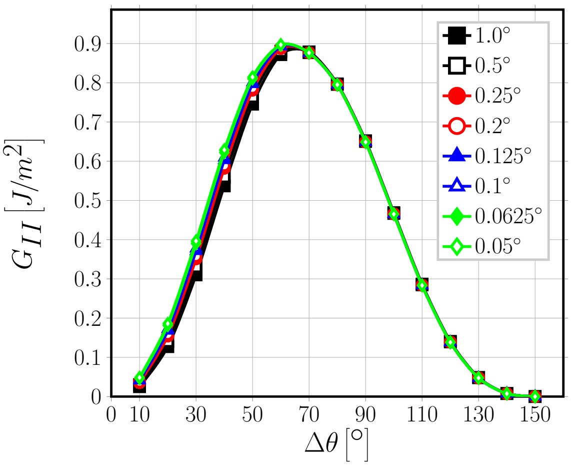

(b) $V_f = 0.1\%$, 2^{nd} order elements.

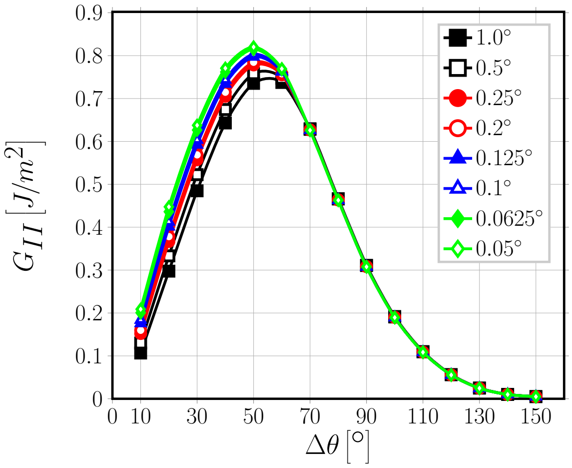

(c) $V_f = 40\%$, 1^{st} order elements.

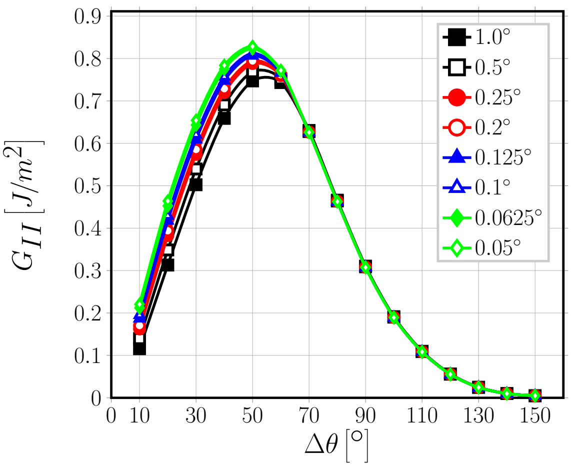

(d) $V_f = 40\%$, 2^{nd} order elements.

Figure 4: Effect of the size δ of an element at the crack tip on Mode II ERR.

2^{nd} order elements.

Analysis of the total ERR in Figure 5 leads to an observation that was not predicted by the considerations of the previous section: G_{TOT} is effectively independent of the element size δ in both the *open* and the *closed* crack regimes, at least for reasonably small elements ($\delta \leq 1.0°$). Given that $G_{II} = G_{TOT}$ for the *closed* crack, it explains the independency of G_{II} from δ after the onset of the contact zone.

Analysis of Fig. 3, Fig. 4 and Fig. 5 has shown the dependency of Mode I and Mode II ERR on the element size δ. Following the derivations of the previous section, we model the dependency of G_I and G_{II} with respect to δ as

$$G_{(\cdot)} = A\left(\Delta\theta\right)\ln\delta + B\left(\Delta\theta\right), \tag{29}$$

where $A\left(\Delta\theta\right)$ and $B\left(\Delta\theta\right)$ are parameters dependent on $\Delta\theta$ estimated through linear regression (with $x = \ln\delta$) of the numerical results.

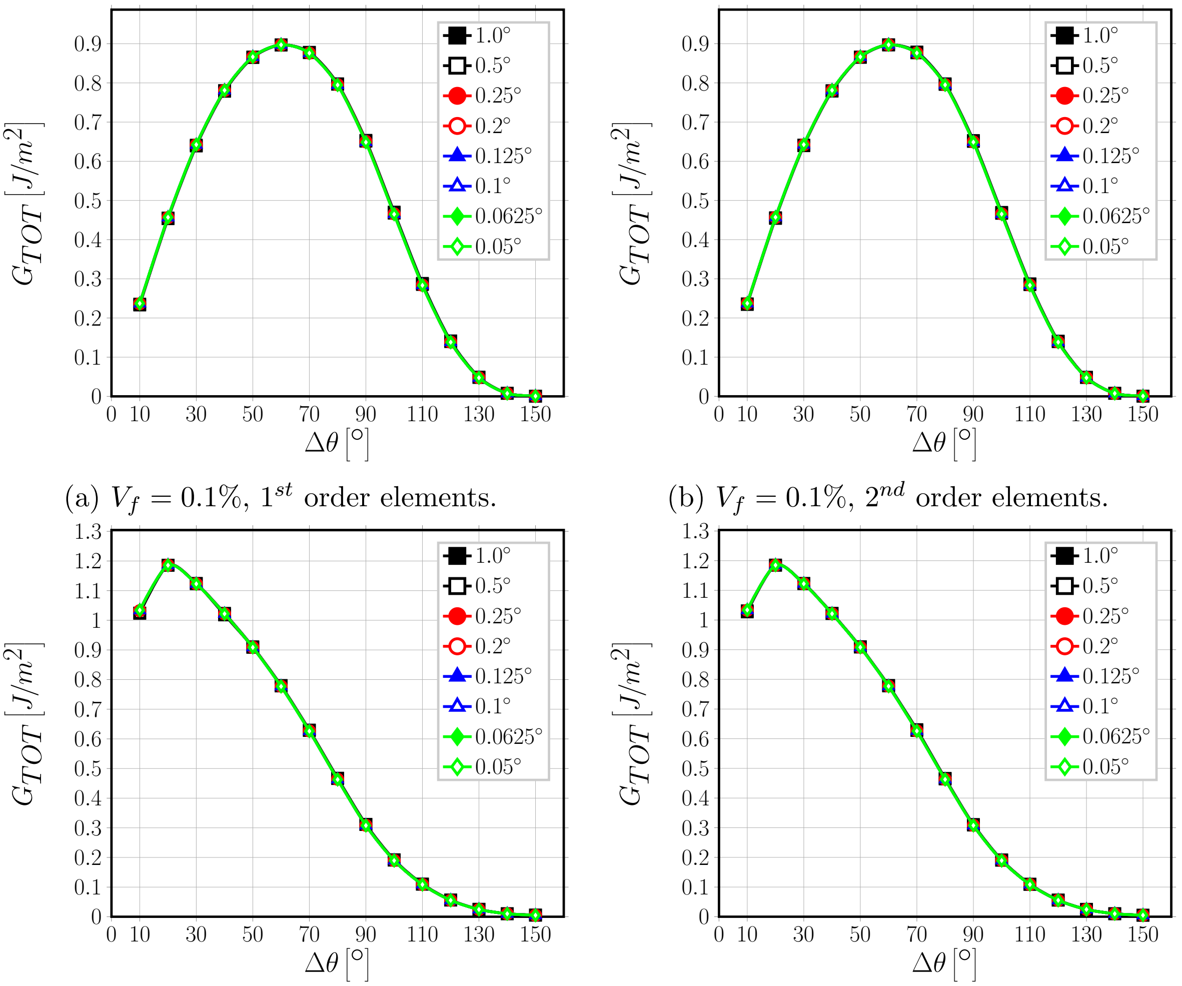

(a) $V_f = 0.1\%$, 1^{st} order elements.

(b) $V_f = 0.1\%$, 2^{nd} order elements.

(c) $V_f = 40\%$, 1^{st} order elements.

(d) $V_f = 40\%$, 2^{nd} order elements.

Figure 5: Effect of the size δ of an element at the crack tip on total ERR.

As shown in Fig. 6, Fig. 7, Fig. 8 and Fig. 9 both in linear and logarithmic scales of δ, the result is remarkable: both the correlation coefficient r and the r^2 ratio (of explained to total variance) are always greater than 0.95 and the p-values of the coefficients A and B are at least $< 1E-6$ and often $< 1E-11$ (see Table 2 for G_I and Table 3 for G_{II}). The results of the linear regression confirm the analytical derivations of the previous section, which showed the logarithmic behavior of Mode I and Mode II ERR. Similar conclusions were reached in [26, 17] for a straight bi-material crack with respect to the parameter $\Delta a/a$; however, no functional expression of $G_{(\cdot)}$ was proposed.

6 Conclusions & Outlook

The application of the Virtual Crack Closure Technique to the calculation of Mode I, Mode II and total Energy Release Rate was analyzed in the context of the Finite Element

Table 2: Summary of linear regression results and main statistical tests for Mode I ERR

$\mathbf{V_f}$ [%]	**Order**	$\mathbf{\Delta\theta}$ [°]	**A** $\left[\frac{\mathbf{J}}{\mathbf{m^2}}\right]$	**B** $\left[\frac{\mathbf{J}}{\mathbf{m^2}}\right]$	**r** [−]	$\mathbf{r^2}$ [−]	**p(A)** [−]	**p(B)** [−]
0.1	1	10.0	0.0064	0.2113	0.9933	0.9866	7.48E-07	3.49E-14
		20.0	0.0183	0.3331	0.9996	0.9992	1.44E-10	2.40E-16
		30.0	0.0280	0.3392	1.0000	1.0000	2.25E-16	4.26E-21
		40.0	0.0304	0.2524	0.9997	0.9995	4.38E-11	7.94E-15
		50.0	0.0235	0.1278	0.9985	0.9970	8.61E-09	2.01E-11
		60.0	0.0094	0.0284	0.9854	0.9709	7.75E-06	6.14E-07
0.1	2	10.0	0.0069	0.2103	0.9962	0.9924	1.36E-07	1.03E-14
		20.0	0.0187	0.3277	0.9997	0.9994	7.85E-11	1.62E-16
		30.0	0.0280	0.3296	1.0000	1.0000	3.28E-16	7.29E-21
		40.0	0.0298	0.2408	0.9997	0.9995	4.82E-11	1.04E-14
		50.0	0.0225	0.1177	0.9984	0.9967	1.10E-08	3.27E-11
		60.0	0.0081	0.0228	0.9811	0.9626	1.66E-05	2.17E-06
40	1	10.0	0.0311	0.9196	0.9963	0.9927	1.03E-07	9.33E-15
		20.0	0.0501	0.8882	1.0000	0.9999	1.21E-13	2.33E-19
		30.0	0.0510	0.6374	0.9998	0.9996	1.66E-11	2.58E-16
		40.0	0.0419	0.3760	0.9988	0.9976	4.56E-09	5.25E-13
		50.0	0.0279	0.1713	0.9980	0.9961	2.22E-08	2.52E-11
		60.0	0.0108	0.0391	0.9901	0.9804	3.44E-06	9.46E-08
40	2	10.0	0.0336	0.9148	0.9988	0.9977	3.45E-09	5.09E-16
		20.0	0.0504	0.8719	1.0000	1.0000	3.70E-14	8.26E-20
		30.0	0.0506	0.6191	0.9999	0.9997	7.63E-12	1.35E-16
		40.0	0.0414	0.3608	0.9994	0.9989	4.95E-10	6.80E-14
		50.0	0.0269	0.1593	0.9982	0.9964	1.66E-08	2.31E-11
		60.0	0.0097	0.0329	0.9890	0.9781	4.96E-06	1.99E-07

solution of the bi-material circular arc crack, or fiber-matrix interface crack. A synthetic vectorial formulation of the VCCT has been proposed and its usefulness exemplified in the analysis of the mesh dependency. By both analytical considerations and numerical simulations, it has been shown that:

- the total ERR is invariant to rotations of the reference frame (and more in general to linear transformations), which implies that rotation of crack tip forces and displacement is actually not required in the use of the VCCT for the calculation of G_{TOT};
- the total ERR does not depend on the size δ of the elements at the crack tip, at least for reasonably small elements ($\delta \leq 1.0°$) ;
- as a consequence, Mode II ERR for the *closed* interface crack does not depend on δ, as $G_{II} = G_{TOT}$ after the onset of the contact zone;

Table 3: Summary of linear regression results and main statistical tests for Mode II ERR

V_f [%]	Order	$\Delta\theta$ [°]	$A\left[\frac{J}{m^2}\right]$	$B\left[\frac{J}{m^2}\right]$	r [−]	r^2 [−]	$p(A)$ [−]	$p(B)$ [−]
0.1	1.0	10.0	-0.0076	0.0228	-0.9996	0.9991	2.09E-10	1.64E-11
		20.0	-0.0194	0.1211	-1.0000	1.0000	1.99E-15	2.02E-18
		30.0	-0.0290	0.3007	-0.9999	0.9998	4.12E-12	1.97E-16
		40.0	-0.0311	0.5270	-0.9995	0.9989	4.13E-10	1.05E-15
		50.0	-0.0240	0.7375	-0.9979	0.9958	2.32E-08	1.66E-15
		60.0	-0.0095	0.8685	-0.9835	0.9672	1.12E-05	1.22E-15
0.1	2.0	10.0	-0.0078	0.0249	-0.9996	0.9992	1.91E-10	1.06E-11
		20.0	-0.0196	0.1272	-1.0000	1.0000	3.48E-15	2.78E-18
		30.0	-0.0288	0.3108	-0.9999	0.9998	1.45E-12	5.47E-17
		40.0	-0.0305	0.5387	-0.9995	0.9990	3.32E-10	6.55E-16
		50.0	-0.0229	0.7478	-0.9979	0.9959	2.17E-08	1.09E-15
		60.0	-0.0082	0.8744	-0.9806	0.9615	1.81E-05	8.26E-16
40.0	1.0	10.0	-0.0344	0.1055	-0.9997	0.9995	3.82E-11	2.73E-12
		20.0	-0.0500	0.2977	-1.0000	0.9999	4.22E-14	5.66E-17
		30.0	-0.0505	0.4866	-0.9999	0.9997	6.44E-12	4.82E-16
		40.0	-0.0420	0.6454	-0.9996	0.9991	2.12E-10	9.66E-16
		50.0	-0.0275	0.7386	-0.9985	0.9971	9.01E-09	1.44E-15
		60.0	-0.0099	0.7402	-0.9926	0.9853	1.41E-06	5.13E-16
40.0	2.0	10.0	-0.0353	0.1145	-0.9998	0.9995	2.92E-11	1.50E-12
		20.0	-0.0504	0.3130	-1.0000	0.9999	4.00E-14	4.17E-17
		30.0	-0.0502	0.5039	-0.9999	0.9998	2.87E-12	1.69E-16
		40.0	-0.0410	0.6615	-0.9996	0.9992	2.02E-10	6.89E-16
		50.0	-0.0263	0.7502	-0.9987	0.9973	6.87E-09	7.76E-16
		60.0	-0.0090	0.7458	-0.9921	0.9842	1.79E-06	3.37E-16

- for the *open* interface crack, Mode I and Mode II ERR depend on the element size δ through a logarithmic law of the type $A(\Delta\theta)\ln\delta + B(\Delta\theta)$;
- the sign of the logarithm is always positive for G_I, i.e. it decreases when δ decreases, and negative for G_{II}, i.e. it increases when δ decreases.

The conclusion is significant: as the behavior of Mode I and Mode II is logarithmic with respect to mesh size, there exists no asymptotic limit and thus no convergence of the values. A convergence analysis based on the reduction of the error between successive iterations would not provide a reliable assessment of the accuracy of the FE solution of Mode I and Mode II Energy Release Rate of the fiber-matrix interface crack. A validation is thus required with respect to data obtained through a different method, be it analytical, numerical or experimental. Moreover, it has been shown that: first, the same behavior appears when using 1^{st} as well as 2^{nd} order elements; second, no improvement is expected with the use of singular elements, as the logarithmic dependency of G_I and G_{II}

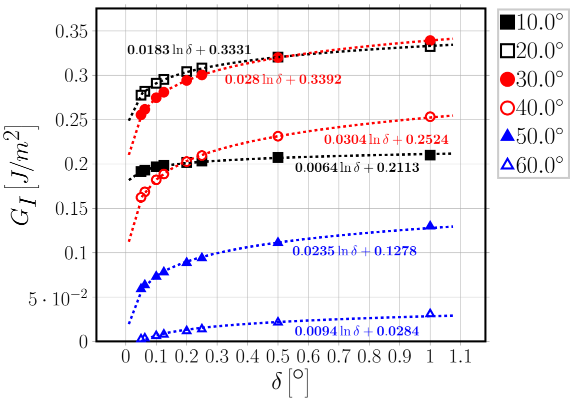

(a) 1^{st} order elements.

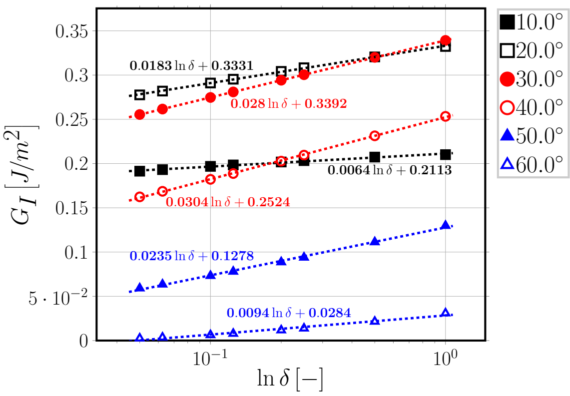

(b) 1^{st} order elements.

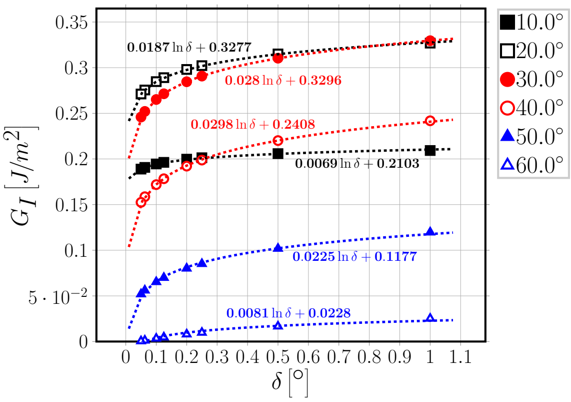

(c) 2^{nd} order elements.

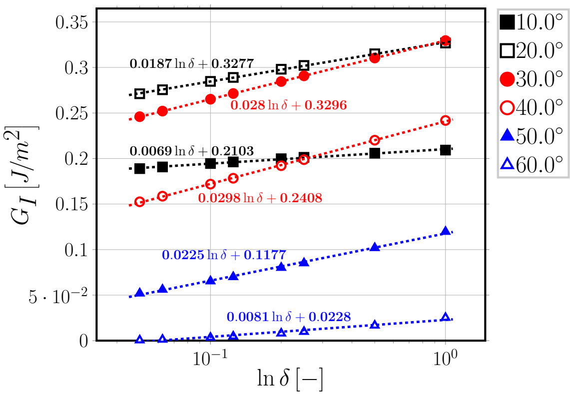

(d) 2^{nd} order elements.

Figure 6: Logarithmic dependence on δ of Mode I ERR: interpolation of numerical results for $V_f = 0.1\%$.

is governed by the definition of ERR itself together with the asymptotic behavior of the displacement field at the crack tip. These two conclusions run contrary to the suggestions provided in the manuals of many commercial FEM packages, such as Abaqus [1] which suggests that (Section 11.4.2 of the *Abaqus Analysis User's Guide*): "*Sharp cracks (where the crack faces lie on top of one another in the undeformed configuration) are usually modeled using small-strain assumptions. Focused meshes, [...], should normally be used for small-strain fracture mechanics evaluations. However, for a sharp crack the strain field becomes singular at the crack tip. [...] In most cases the singularity at the crack tip should be considered in small-strain analysis (when geometric nonlinearities are ignored). Including the singularity often improves the accuracy of the J-integral, the stress intensity factors, and the stress and strain calculations because the stresses and strains in the region close to the crack tip are more accurate.*". We have shown that, in the context of the fiber/matrix interface crack, the convergence of the Energy Release Rate is determined by the asymptotic behavior of the elastic solution and only marginally by the choice of element order and type, thus contradicting the statements in [1].

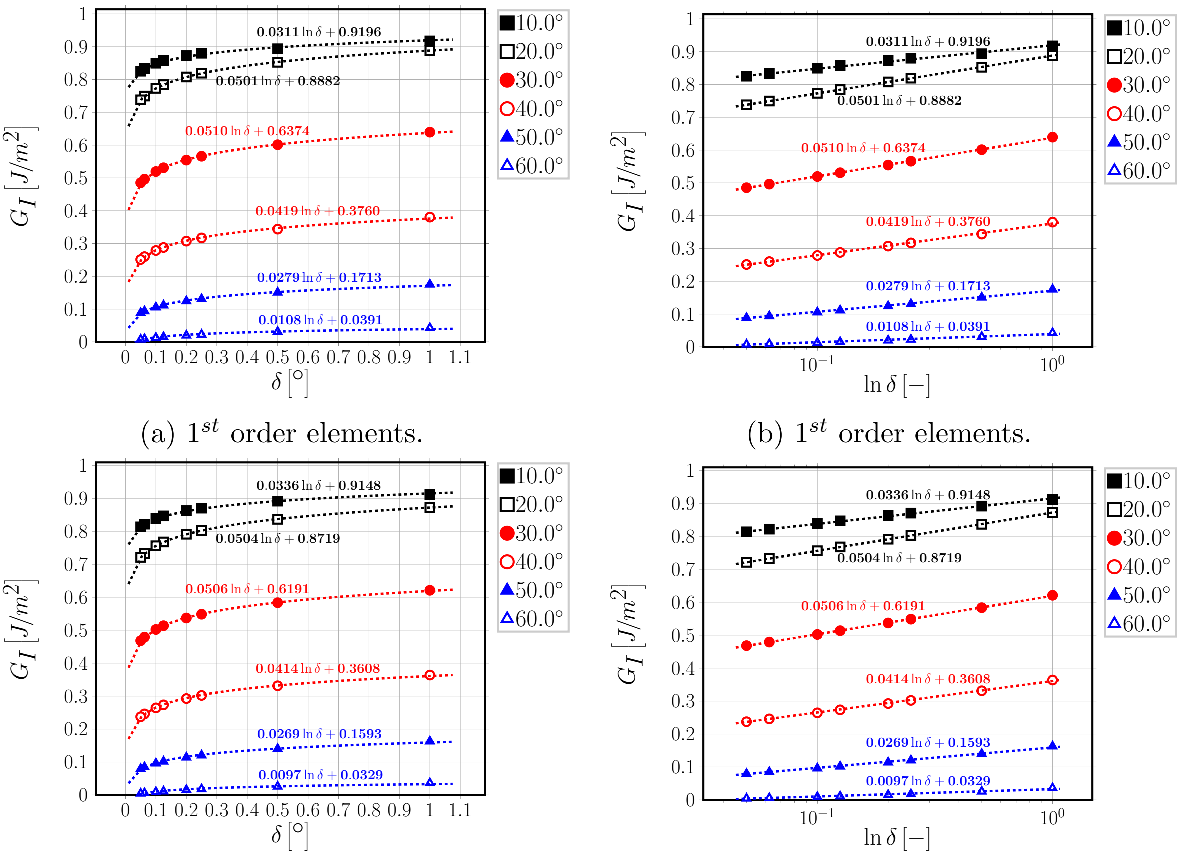

(a) 1^{st} order elements. (b) 1^{st} order elements.

(c) 2^{nd} order elements. (d) 2^{nd} order elements.

Figure 7: Logarithmic dependence on δ of Mode I ERR: interpolation of numerical results for $V_f = 40\%$.

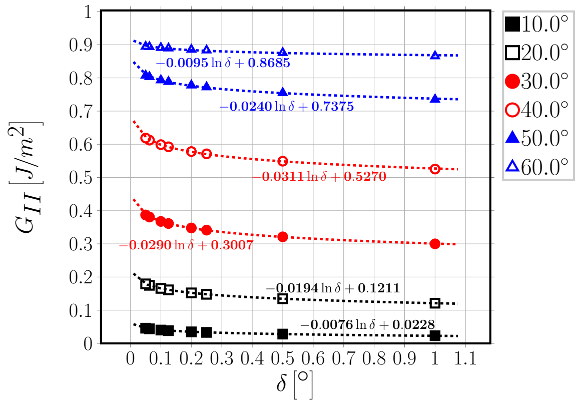

(a) 1^{st} order elements.

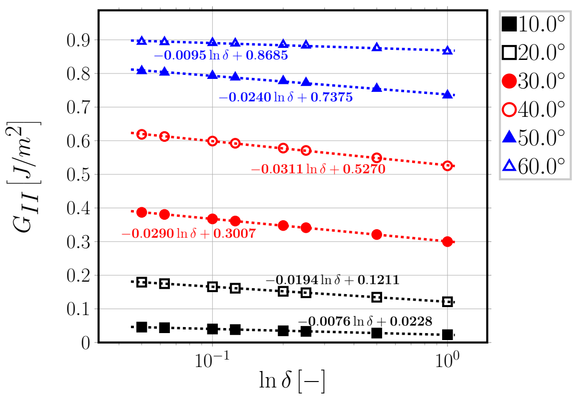

(b) 1^{st} order elements.

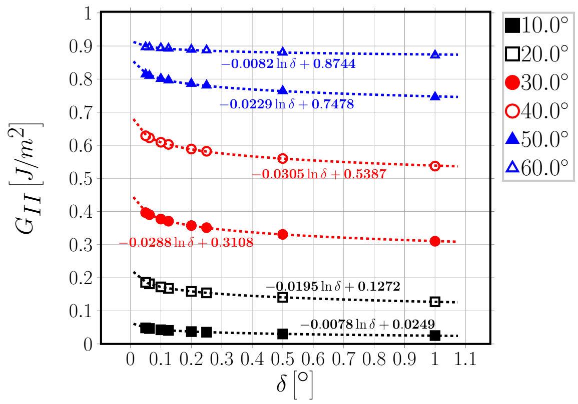

(c) 2^{nd} order elements.

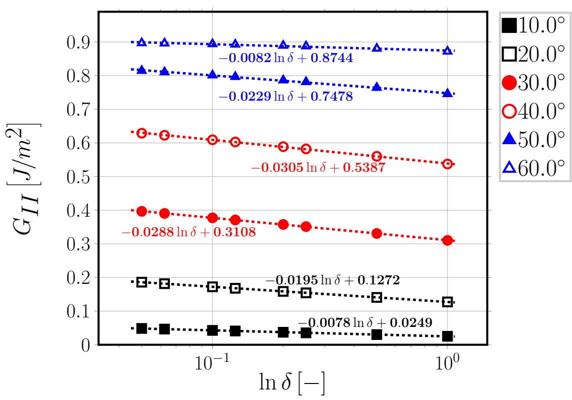

(d) 2^{nd} order elements.

Figure 8: Logarithmic dependence on δ of Mode II ERR: interpolation of numerical results for $V_f = 0.1\%$.

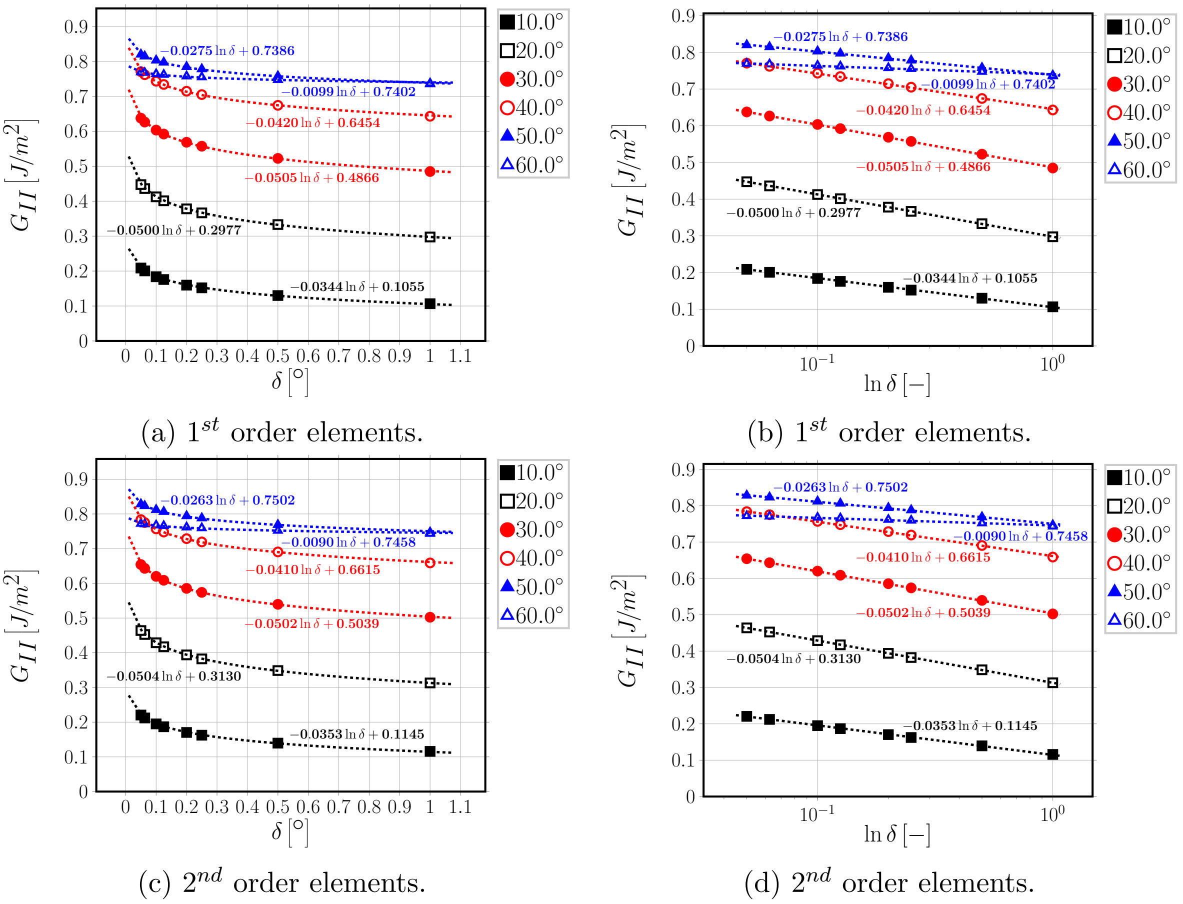

(a) 1^{st} order elements.

(b) 1^{st} order elements.

(c) 2^{nd} order elements.

(d) 2^{nd} order elements.

Figure 9: Logarithmic dependence on δ of Mode II ERR: interpolation of numerical results for $V_f = 40\%$.

Acknowledgements

Luca Di Stasio thanks Prof. Janis Varna for the useful discussions and suggestions. Luca Di Stasio gratefully acknowledges the support of the European School of Materials (EUSMAT) through the DocMASE Doctoral Programme and the European Commission through the Erasmus Mundus Programme.

References

[1] *ABAQUS/Standard User's Manual, Version 6.12*. Simulia. Providence, RI, USA, 2012.

[2] J. C. Del Caño and F. París. "On stress singularities induced by the discretization in curved receding contact surfaces: a BEM analysis". In: *International Journal for Numerical Methods in Engineering* 40.12 (June 1997), pp. 2301–2320. DOI: `10.1002/(sici)1097-0207(19970630)40:12<2301::aid-nme166>3.0.co;2-8`.

[3] Maria Comninou. "An overview of interface cracks". In: *Engineering Fracture Mechanics* 37.1 (Jan. 1990), pp. 197–208. DOI: `10.1016/0013-7944(90)90343-f`.

[4] Maria Comninou. "The Interface Crack". In: *Journal of Applied Mechanics* 44.4 (1977), p. 631. DOI: `10.1115/1.3424148`. URL: `https://doi.org/10.1115/1.3424148`.

[5] E. Correa, V. Mantič, and F. París. "Effect of thermal residual stresses on matrix failure under transverse tension at micromechanical level: A numerical and experimental analysis". In: *Composites Science and Technology* 71.5 (Mar. 2011), pp. 622–629. DOI: `10.1016/j.compscitech.2010.12.027`.

[6] E. Correa, F. París, and V. Mantič. "Effect of a secondary transverse load on the inter-fibre failure under compression". In: *Composites Part B: Engineering* 65 (Oct. 2014), pp. 57–68. DOI: `10.1016/j.compositesb.2014.01.005`.

[7] E. Correa, F. París, and V. Mantič. "Effect of the presence of a secondary transverse load on the inter-fibre failure under tension". In: *Engineering Fracture Mechanics* 103 (May 2013), pp. 174–189. DOI: `10.1016/j.engfracmech.2013.02.026`.

[8] E. Correa et al. "Effects of the presence of compression in transverse cyclic loading on fibre–matrix debonding in unidirectional composite plies". In: *Composites Part A: Applied Science and Manufacturing* 38.11 (Nov. 2007), pp. 2260–2269. DOI: `10.1016/j.compositesa.2006.11.002`.

[9] J. Dundurs. "Discussion: "Edge-Bonded Dissimilar Orthogonal Elastic Wedges Under Normal and Shear Loading" (Bogy, D. B., 1968, ASME J. Appl. Mech., 35, pp. 460–466)". In: *Journal of Applied Mechanics* 36.3 (1969), p. 650. DOI: `10.1115/1.3564739`.

[10] A. H. England. "A Crack Between Dissimilar Media". In: *Journal of Applied Mechanics* 32.2 (1965), p. 400. DOI: `10.1115/1.3625813`.

[11] A. H. England. “An Arc Crack Around a Circular Elastic Inclusion”. In: *Journal of Applied Mechanics* 33.3 (1966), p. 637. DOI: 10.1115/1.3625132.

[12] Fazil Erdogan. “Stress Distribution in a Nonhomogeneous Elastic Plane With Cracks”. In: *Journal of Applied Mechanics* 30.2 (1963), p. 232. DOI: 10.1115/1.3636517.

[13] D.A. Hills and J.R. Barber. “Interface cracks”. In: *International Journal of Mechanical Sciences* 35.1 (Jan. 1993), pp. 27–37. DOI: 10.1016/0020-7403(93)90062-y.

[14] George R. Irwin. “Fracture”. In: *Elasticity and Plasticity / Elastizität und Plastizität*. Springer Berlin Heidelberg, 1958, pp. 551–590. DOI: 10.1007/978-3-642-45887-3_5.

[15] Ronald Krueger. “Virtual crack closure technique: History, approach, and applications”. In: *Applied Mechanics Reviews* 57.2 (2004), p. 109. DOI: 10.1115/1.1595677.

[16] B.M. Malyshev and R.L. Salganik. “The strength of adhesive joints using the theory of cracks”. In: *International Journal of Fracture Mechanics* 1-1.2 (June 1965). DOI: 10.1007/bf00186749. URL: https://doi.org/10.1007/bf00186749.

[17] M.G. Manoharan and C.T. Sun. “Strain energy release rates of an interfacial crack between two anisotropic solids under uniform axial strain”. In: *Composites Science and Technology* 39.2 (Jan. 1990), pp. 99–116. DOI: 10.1016/0266-3538(90)90049-b.

[18] F. París, J. C. Caño, and J. Varna. “The fiber-matrix interface crack — A numerical analysis using Boundary Elements”. In: *International Journal of Fracture* 82.1 (May 1996), pp. 11–29. DOI: 10.1007/bf00017861.

[19] Federico París, Elena Correa, and Vladislav Mantič. “Kinking of Transversal Interface Cracks Between Fiber and Matrix”. In: *Journal of Applied Mechanics* 74.4 (2007), p. 703. DOI: 10.1115/1.2711220.

[20] A.B. Perlman and G.C. Sih. “Elastostatic problems of curvilinear cracks in bonded dissimilar materials”. In: *International Journal of Engineering Science* 5.11 (Nov. 1967), pp. 845–867. DOI: 10.1016/0020-7225(67)90009-2.

[21] I.S. Raju. “Calculation of strain-energy release rates with higher order and singular finite elements”. In: *Engineering Fracture Mechanics* 28.3 (Jan. 1987), pp. 251–274. DOI: 10.1016/0013-7944(87)90220-7.

[22] E.F. Rybicki and M.F. Kanninen. “A finite element calculation of stress intensity factors by a modified crack closure integral”. In: *Engineering Fracture Mechanics* 9.4 (Jan. 1977), pp. 931–938. DOI: 10.1016/0013-7944(77)90013-3.

[23] C. Sandino, E. Correa, and F. París. “Interface crack growth under transverse compression: nearby fibre effect”. In: *Proceeding of the 18^{th} European Conference on Composite Materials (ECCM-18).* (Athens, Greece, June 24–28, 2018). 2018.

[24] C. Sandino, E. Correa, and F. París. "Numerical analysis of the influence of a nearby fibre on the interface crack growth in composites under transverse tensile load". In: *Engineering Fracture Mechanics* 168 (Dec. 2016), pp. 58–75. DOI: 10.1016/j.engfracmech.2016.01.022.

[25] C.T. Sun and W. Qian. "The use of finite extension strain energy release rates in fracture of interfacial cracks". In: *International Journal of Solids and Structures* 34.20 (July 1997), pp. 2595–2609. DOI: 10.1016/s0020-7683(96)00157-6.

[26] C.T Sun and C.J Jih. "On strain energy release rates for interfacial cracks in bi-material media". In: *Engineering Fracture Mechanics* 28.1 (Jan. 1987), pp. 13–20. DOI: 10.1016/0013-7944(87)90115-9.

[27] M. Toya. "A crack along the interface of a circular inclusion embedded in an infinite solid". In: *Journal of the Mechanics and Physics of Solids* 22.5 (Oct. 1974), pp. 325–348. DOI: 10.1016/0022-5096(74)90002-7.

[28] Paolo S. Valvo. "A revised virtual crack closure technique for physically consistent fracture mode partitioning". In: *International Journal of Fracture* 173.1 (Dec. 2011), pp. 1–20. DOI: 10.1007/s10704-011-9658-y.

[29] J. Varna, Federico París, and J. C.Caño. "The effect of crack-face contact on fiber/matrix debonding in transverse tensile loading". In: *Composites Science and Technology* 57.5 (1997), pp. 523–532. DOI: 10.1016/s0266-3538(96)00175-3.

[30] Janis Varna et al. "Growth and Interaction of Debonds in Local Clusters of Fibers in Unidirectional Composites during Transverse Loading". In: *Key Engineering Materials* 754 (Sept. 2017), pp. 63–66. DOI: 10.4028/www.scientific.net/kem.754.63.

[31] M. L. Williams. "The stresses around a fault or crack in dissimilar media". In: *Bulletin of the Seismological Society of America* 49.2 (1959), p. 199.

[32] Linqi Zhuang, Ramesh Talreja, and Janis Varna. "Transverse crack formation in unidirectional composites by linking of fibre/matrix debond cracks". In: *Composites Part A: Applied Science and Manufacturing* 107 (Apr. 2018), pp. 294–303. DOI: 10.1016/j.compositesa.2018.01.013.

[33] Linqi Zhuang et al. "Effects of inter-fiber spacing on fiber-matrix debond crack growth in unidirectional composites under transverse loading". In: *Composites Part A: Applied Science and Manufacturing* 109 (June 2018), pp. 463–471. DOI: 10.1016/j.compositesa.2018.03.031.

A Derivation of the relationship between crack tip forces and displacements for first order quadrilateral elements

A.1 Foundational relations

In the isoparametric formulation of the Finite Element Method, the element Jacobian J and its inverse J^{-1} can be expressed in general as

$$\underline{\underline{J}} = \left[\underline{e}_\xi | \underline{e}_\eta\right] = \begin{bmatrix} \frac{\partial x}{\partial \xi} & \frac{\partial x}{\partial \eta} \\ \frac{\partial y}{\partial \xi} & \frac{\partial y}{\partial \eta} \end{bmatrix} \qquad \underline{\underline{J}}^{-1} = \left[\underline{e}^x | \underline{e}^y\right] = \begin{bmatrix} \frac{\partial \xi}{\partial x} & \frac{\partial \xi}{\partial y} \\ \frac{\partial \eta}{\partial x} & \frac{\partial \eta}{\partial y} \end{bmatrix} \tag{A.30}$$

where $\{e_\xi, e_\eta\}$ and $\{e^x, e^y\}$ are respectively the covariant and contravariant basis vectors of the mapping between global $\{x, y\}$ and local element $\{\xi, \eta\}$ coordinates:

$$\underline{e}_\xi = \begin{bmatrix} \frac{\partial x}{\partial \xi} \\ \frac{\partial y}{\partial \xi} \end{bmatrix} \quad \underline{e}_\eta = \begin{bmatrix} \frac{\partial x}{\partial \eta} \\ \frac{\partial y}{\partial \eta} \end{bmatrix}, \tag{A.31}$$

$$\underline{e}_x = \begin{bmatrix} \frac{\partial \xi}{\partial x} \\ \frac{\partial \eta}{\partial x} \end{bmatrix} \quad \underline{e}_y = \begin{bmatrix} \frac{\partial \xi}{\partial y} \\ \frac{\partial \eta}{\partial y} \end{bmatrix}. \tag{A.32}$$

Denoting by d the number of geometrical dimensions of the problem ($d = 2$ in the present work) and by $\underline{p}$ the $d \times 1$ position vector in global coordinates, we can formally introduce the $3\,(d-1) \times d$ matrix operator of partial differentiation $\underline{\underline{\widetilde{B}}}$ such that

$$\underline{\varepsilon}\left(\underline{p}\right) = \underline{\underline{\widetilde{B}}} \cdot \underline{u}\left(\underline{p}\right), \tag{A.33}$$

where $\underline{u}$ and $\underline{\varepsilon}$ are respectively the $d \times 1$ displacement vector and the $3\,(d-1) \times 1$ strain vector in Voigt notation. Denoting by n the number of nodes of a generic element ($n = s \times m$ where s represents the number of sides of the element and m the order of the shape functions), we can furthermore introduce the $d \times d \cdot n$ matrix $\underline{\underline{\mathrm{N}}}$ of shape functions such that

$$\underline{u} = \underline{\underline{N}} \cdot \underline{u}_N, \tag{A.34}$$

where $\underline{u}_N$ is the $d \cdot n \times 1$ vector of element nodal variables. Having introduced $\underline{\underline{\widetilde{B}}}$ and $\underline{\underline{N}}$ in Equations A.33 and A.34 respectively, it is possible to define the $3\,(d-1) \times d \cdot n$ matrix $\underline{\underline{B}}$ of derivatives (with respect to global coordinates) of shape functions as

$$\underline{\underline{B}} = \underline{\underline{\widetilde{B}}} \cdot \underline{\underline{N}}. \tag{A.35}$$

We introduce the linear elastic material behavior in the form of the $3\,(d-1) \times 3\,(d-1)$ rigidity matrix $\underline{\underline{D}}$ such that

$$\underline{\sigma} = \underline{\underline{D}} \cdot \underline{\varepsilon}, \tag{A.36}$$

where $\underline{\sigma}$ the $3\left(d-1\right)\times 1$ stress vector in Voigt notation. It is finally possible to define the $n \times n$ element stiffness matrix $\underline{\underline{k_e}}$ as

$$\underline{\underline{k_e}} = \int_{V_e(x,y)} \left(\underline{\underline{B}}^T \underline{\underline{D}} \cdot \underline{\underline{B}}\right) dV_e\left(x,\dots,y\right) = \int_{V_e(\xi,\eta)} \left(\underline{\underline{B}}^T \underline{\underline{D}} \cdot \underline{\underline{B}}\right) \sqrt{g} dV_e\left(\xi,\dots,\eta\right), \tag{A.37}$$

where $g = det\left(\underline{\underline{J}}^T \underline{\underline{J}}\right)$ and V_e is the element volume. Given that isoparametric elements are always defined between -1 and 1 in each dimension, Equation A.37 can simplified to

$$\underline{\underline{k_e}} = \int_{-1}^{1} \cdots \int_{-1}^{1} \left(\underline{\underline{B}}^T \underline{\underline{D}} \cdot \underline{\underline{B}}\right) \sqrt{g} d\xi, \dots, d\eta, \tag{A.38}$$

which is amenable to numerical integration by means of a Gaussian quadrature of the form

$$\underline{\underline{k_e}} \approx \sum_{i=1}^{N} \cdots \sum_{j=1}^{N} w_i \dots w_j \left(\underline{\underline{B}}^T\left(\xi_i,\dots,\eta_j\right) \cdot \underline{\underline{D}} \cdot \underline{\underline{B}}\left(\xi_i,\dots,\eta_j\right)\sqrt{g}\right), \tag{A.39}$$

where $\left(\xi_i,\dots,\eta_j\right)$ are the coordinates of the N Gaussian quadrature points. The element stiffness matrix as evaluated in Eq. A.39 is in general a full symmetric (in the case of linear elasticity) matrix of the form

$$k_e = \begin{bmatrix} k_{e|11} & k_{e|12} & k_{e|13} & k_{e|14} & k_{e|15} & k_{e|16} & k_{e|17} & k_{e|18} \\ k_{e|12} & k_{e|22} & k_{e|23} & k_{e|24} & k_{e|25} & k_{e|26} & k_{e|27} & k_{e|28} \\ k_{e|13} & k_{e|23} & k_{e|33} & k_{e|34} & k_{e|35} & k_{e|36} & k_{e|37} & k_{e|38} \\ k_{e|14} & k_{e|24} & k_{e|34} & k_{e|44} & k_{e|45} & k_{e|46} & k_{e|47} & k_{e|48} \\ k_{e|15} & k_{e|25} & k_{e|35} & k_{e|45} & k_{e|55} & k_{e|56} & k_{e|57} & k_{e|58} \\ k_{e|16} & k_{e|26} & k_{e|36} & k_{e|46} & k_{e|56} & k_{e|66} & k_{e|67} & k_{e|68} \\ k_{e|17} & k_{e|27} & k_{e|37} & k_{e|47} & k_{e|57} & k_{e|67} & k_{e|77} & k_{e|78} \\ k_{e|18} & k_{e|28} & k_{e|38} & k_{e|48} & k_{e|58} & k_{e|68} & k_{e|78} & k_{e|88} \end{bmatrix}. \tag{A.40}$$

A.2 Calculation of displacements and reaction forces

With reference to Fig. 10, we define:

$u_{x,M}$, $u_{x,F}$ the x-displacement of the nodes belonging to the free side of the first element belonging to the crack, respectively on the matrix (bulk) and fiber (inclusion) side;

$u_{y,M}$, $u_{y,F}$ the y-displacement of the nodes belonging to the free side of the first element belonging to the crack, respectively on the matrix (bulk) and fiber (inclusion) side;

$u_{r,M}$, $u_{r,F}$ the x-displacement of the nodes belonging to the free side of the first element belonging to the crack, respectively on the matrix (bulk) and fiber (inclusion) side;

$u_{\theta,M}$, $u_{\theta,F}$ the y-displacement of the nodes belonging to the free side of the first element belonging to the crack, respectively on the matrix (bulk) and fiber (inclusion) side;

$F_{x,CT}$, $F_{y,CT}$ respectively the x- and y-component of the reaction force at the crack tip;

$F_{r,CT}$, $F_{\theta,CT}$ respectively the r- and θ-component of the reaction force at the crack tip.

The $x-y$ reference frame is the global reference frame, while the $r-\theta$ reference frame is such that the θ direction coincides with the crack propagation direction at the crack tip and r the in-plane normal to the propagation direction. For an arc-crack as the present one, the r-direction coincides with the radial direction of the inclusion.

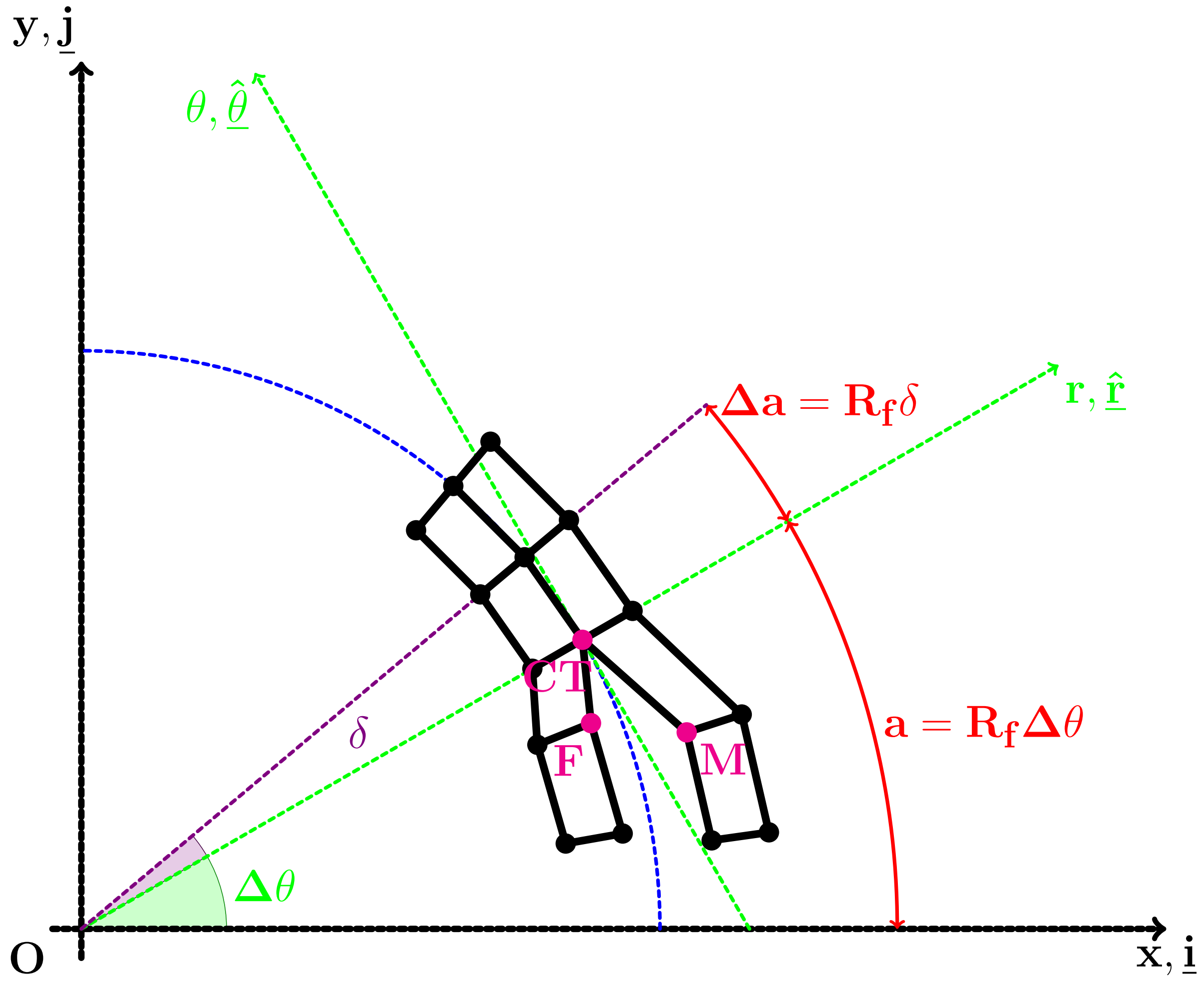

Figure 10: Schematic representation of the discretized crack tip geometry for 1^{st} *order quadrilateral elements.*

The crack opening displacement u_r and the crack shear displacement u_θ at the crack tip can thus be written as

$$u_r = \cos(\Delta\theta)\, u_x + \sin(\Delta\theta)\, u_y \qquad u_\theta = -\sin(\Delta\theta)\, u_x + \cos(\Delta\theta)\, u_y, \tag{A.41}$$

where u_x and u_y are defined as

$$u_x = u_{x,M} - u_{x,F} \qquad u_y = u_{y,M} - u_{y,F} \tag{A.42}$$

and $2\Delta\theta$ is total angular size of the debond. The corresponding forces at the crack tip are

$$F_r = \cos(\Delta\theta) F_{x,CT} + \sin(\Delta\theta) F_{y,CT} \qquad F_\theta = -\sin(\Delta\theta) F_{x,CT} + \cos(\Delta\theta) F_{y,CT}. \tag{A.43}$$

At the crack tip, the FE mesh possesses two coincident points, labeled FCT and MCT. Continuity of the displacements at the crack tip must be ensured. Furthermore, in order to measure the force at the crack tip, a fully-constraint dummy node needs to be created and formally linked to the two nodes at the crack tip by the conditions

$$\begin{cases} u_{x,FCT} - u_{x,MCT} - u_{x,DUMMY} = 0 \\ u_{y,FCT} - u_{y,MCT} - u_{y,DUMMY} = 0 \\ u_{x,DUMMY} = 0 \\ u_{y,DUMMY} = 0 \end{cases}, \tag{A.44}$$

which can be simplified to

$$\begin{cases} u_{x,FCT} = u_{x,MCT} \\ u_{y,FCT} = u_{y,MCT} \\ R_{x,DUMMY} = R_{x,FCT} = -R_{x,MCT} = F_{x,CT} \\ R_{y,DUMMY} = R_{y,FCT} = -R_{y,MCT} = F_{y,CT} \end{cases}. \tag{A.45}$$

Making use of Eq. A.40, four equations can be written in the four displacement $u_{x,FCT}$, $u_{x,MCT}$, $u_{y,FCT}$ and $u_{y,MCT}$:

$$\begin{cases} \left(k_{e,M|11}+k_{e,M|33}\right)u_{x,MCT}+\left(k_{e,M|12}+k_{e,M|34}\right)u_{y,MCT}+ \\ +k_{e,M|13}u_{x,M}+k_{e,M|14}u_{y,M}+\left(k_{M|17}+k_{M|35}\right)u_{N,MC|7}+\left(k_{M|18}+k_{M|36}\right)u_{N,MC|8}+ \\ +\sum_{i=5}^{6}k_{M|1i}u_{N,MC|i}+\sum_{i=7}^{8}k_{M|3i}u_{N,MB|i}+k_{M|31}u_{x,NCOI}+k_{M|32}u_{y,NCOI}=0 \\ \left(k_{e,M|21}+k_{e,M|43}\right)u_{x,MCT}+\left(k_{e,M|22}+k_{e,M|44}\right)u_{y,MCT}+ \\ +k_{e,M|23}u_{x,M}+k_{e,M|24}u_{y,M}+\left(k_{M|27}+k_{M|45}\right)u_{N,MC|7}+\left(k_{M|28}+k_{M|46}\right)u_{N,MC|8}+ \\ +\sum_{i=5}^{6}k_{M|2i}u_{N,MC|i}+\sum_{i=7}^{8}k_{M|4i}u_{N,MB|i}+k_{M|41}u_{x,NCOI}+k_{M|42}u_{y,NCOI}=0 \\ \left(k_{e,F|77}+k_{e,F|55}\right)u_{x,FCT}+\left(k_{e,F|78}+k_{e,F|56}\right)u_{y,FCT}+ \\ +k_{e,F|75}u_{x,F}+k_{e,F|76}u_{y,F}+\left(k_{F|71}+k_{F|53}\right)u_{N,FC|1}+\left(k_{F|72}+k_{F|54}\right)u_{N,FC|2}+ \\ +\sum_{i=2}^{3}k_{F|7i}u_{N,FC|i}+\sum_{i=1}^{2}k_{F|5i}u_{N,FB|i}+k_{F|57}u_{x,NCOI}+k_{F|58}u_{y,NCOI}=0 \\ \left(k_{e,F|87}+k_{e,F|65}\right)u_{x,FCT}+\left(k_{e,F|88}+k_{e,F|66}\right)u_{y,FCT}+ \\ +k_{e,F|85}u_{x,F}+k_{e,F|86}u_{y,F}+\left(k_{F|81}+k_{F|63}\right)u_{N,FC|1}+\left(k_{F|82}+k_{F|64}\right)u_{N,FC|2}+ \\ +\sum_{i=2}^{3}k_{F|8i}u_{N,FC|i}+\sum_{i=1}^{2}k_{F|6i}u_{N,FB|i}+k_{F|67}u_{x,NCOI}+k_{F|68}u_{y,NCOI}=0 \end{cases}. \tag{A.46}$$

Solving for $u_{y,FCT}$ and $u_{y,MCT}$ the third and fourth relations in Eq. A.46 and substituting in the first two expressions of Eq. A.46, we get

$$\begin{cases} \left(k_{e,M|11}+k_{e,M|33}+k_{e,F|77}+k_{e,F|55}\right)u_{x,MCT}+\left(k_{e,M|12}+k_{e,M|34}+k_{e,F|78}+k_{e,F|56}\right)u_{y,MCT}+ \\ +k_{e,M|13}u_{x,M}+k_{e,M|14}u_{y,M}+k_{e,F|75}u_{x,F}+k_{e,F|76}u_{y,F}+ \\ +\left(k_{M|31}+k_{F|57}\right)u_{x,NCOI}+\left(k_{M|32}+k_{F|58}\right)u_{y,NCOI}+ \\ +\left(k_{M|17}+k_{M|35}\right)u_{N,MC|7}+\left(k_{M|18}+k_{M|36}\right)u_{N,MC|8}+\left(k_{F|71}+k_{F|53}\right)u_{N,FC|1}+\left(k_{F|72}+k_{F|54}\right)u_{N,FC|2}+ \\ +\sum_{i=5}^{6}k_{M|1i}u_{N,MC|i}+\sum_{i=7}^{8}k_{M|3i}u_{N,MB|i}+\sum_{i=2}^{3}k_{F|7i}u_{N,FC|i}+\sum_{i=1}^{2}k_{F|5i}u_{N,FB|i}=0 \\ \left(k_{e,M|21}+k_{e,M|43}+k_{e,F|87}+k_{e,F|65}\right)u_{x,MCT}+\left(k_{e,M|22}+k_{e,M|44}+k_{e,F|88}+k_{e,F|66}\right)u_{y,MCT}+ \\ +k_{e,M|23}u_{x,M}+k_{e,M|24}u_{y,M}+k_{e,F|85}u_{x,F}+k_{e,F|86}u_{y,F}+ \\ +\left(k_{M|41}+k_{F|67}\right)u_{x,NCOI}+\left(k_{M|42}+k_{F|68}\right)u_{y,NCOI}+ \\ +\left(k_{M|27}+k_{M|45}\right)u_{N,MC|7}+\left(k_{M|28}+k_{M|46}\right)u_{N,MC|8}+\left(k_{F|81}+k_{F|63}\right)u_{N,FC|1}+\left(k_{F|82}+k_{F|64}\right)u_{N,FC|2}+ \\ +\sum_{i=2}^{3}k_{F|8i}u_{N,FC|i}+\sum_{i=1}^{2}k_{F|6i}u_{N,FB|i}+\sum_{i=5}^{6}k_{M|2i}u_{N,MC|i}+\sum_{i=7}^{8}k_{M|4i}u_{N,MB|i}=0 \end{cases} \tag{A.47}$$

Solving the system of two equations and observing that $u_{x,F}, u_{y,F} \sim 0$ for a stiffer inclusion as a fiber in a polymeric composite, we can express $u_{x,MCT}$ as a function of u_x and u_y (see Eq. A.42) as

$$
\begin{aligned}
&\left[\left(k_{e,M|21}+k_{e,M|43}+k_{e,F|87}+k_{e,F|65}\right)+\frac{k_{e,M|11}+k_{e,M|33}+k_{e,F|77}+k_{e,F|55}}{k_{e,M|12}+k_{e,M|34}+k_{e,F|78}+k_{e,F|56}}\left(k_{e,M|22}+k_{e,M|44}+k_{e,F|88}+k_{e,F|66}\right)\right]u_{x,MCT}+\\
&+\left(k_{e,M|23}-\frac{k_{e,M|22}+k_{e,M|44}+k_{e,F|88}+k_{e,F|66}}{k_{e,M|12}+k_{e,M|34}+k_{e,F|78}+k_{e,F|56}}k_{e,M|13}\right)u_x+\\
&+\left(k_{e,M|24}-\frac{k_{e,M|22}+k_{e,M|44}+k_{e,F|88}+k_{e,F|66}}{k_{e,M|12}+k_{e,M|34}+k_{e,F|78}+k_{e,F|56}}k_{e,M|14}\right)u_y+\\
&+\left(k_{e,M|23}+k_{e,F|85}-\frac{k_{e,M|22}+k_{e,M|44}+k_{e,F|88}+k_{e,F|66}}{k_{e,M|12}+k_{e,M|34}+k_{e,F|78}+k_{e,F|56}}\left(k_{e,M|13}+k_{e,M|75}\right)\right)\cancelto{\approx 0}{u_{x,F}}+\\
&+\left(k_{e,M|24}+k_{e,F|86}-\frac{k_{e,M|22}+k_{e,M|44}+k_{e,F|88}+k_{e,F|66}}{k_{e,M|12}+k_{e,M|34}+k_{e,F|78}+k_{e,F|56}}\left(k_{e,M|14}+k_{e,M|76}\right)\right)\cancelto{\approx 0}{u_{y,F}}+\\
&+\left[\left(k_{M|41}+k_{F|67}\right)-\frac{k_{e,M|22}+k_{e,M|44}+k_{e,F|88}+k_{e,F|66}}{k_{e,M|12}+k_{e,M|34}+k_{e,F|78}+k_{e,F|56}}\left(k_{M|31}+k_{F|57}\right)\right]u_{x,NCOI}+\\
&+\left[\left(k_{M|42}+k_{F|68}\right)-\frac{k_{e,M|22}+k_{e,M|44}+k_{e,F|88}+k_{e,F|66}}{k_{e,M|12}+k_{e,M|34}+k_{e,F|78}+k_{e,F|56}}\left(k_{M|32}+k_{F|58}\right)\right]u_{y,NCOI}+\\
&+\left(k_{M|27}+k_{M|45}\right)u_{N,MC|7}+\left(k_{M|28}+k_{M|46}\right)u_{N,MC|8}+\left(k_{F|81}+k_{F|63}\right)u_{N,FC|1}+\left(k_{F|82}+k_{F|64}\right)u_{N,FC|2}+\\
&-\frac{k_{e,M|22}+k_{e,M|44}+k_{e,F|88}+k_{e,F|66}}{k_{e,M|12}+k_{e,M|34}+k_{e,F|78}+k_{e,F|56}}\left[\left(k_{M|17}+k_{M|35}\right)u_{N,MC|7}+\left(k_{M|18}+k_{M|36}\right)u_{N,MC|8}\right]+\\
&-\frac{k_{e,M|22}+k_{e,M|44}+k_{e,F|88}+k_{e,F|66}}{k_{e,M|12}+k_{e,M|34}+k_{e,F|78}+k_{e,F|56}}\left[\left(k_{F|71}+k_{F|53}\right)u_{N,FC|1}+\left(k_{F|72}+k_{F|54}\right)u_{N,FC|2}\right]\\
&+\sum_{i=2}^{3}k_{F|8i}u_{N,FC|i}+\sum_{i=1}^{2}k_{F|6i}u_{N,FB|i}+\sum_{i=5}^{6}k_{M|2i}u_{N,MC|i}+\sum_{i=7}^{8}k_{M|4i}u_{N,MB|i}+\\
&-\frac{\sum_{i=5}^{6}k_{M|1i}u_{N,MC|i}+\sum_{i=7}^{8}k_{M|3i}u_{N,MB|i}+\sum_{i=2}^{3}k_{F|7i}u_{N,FC|i}+\sum_{i=1}^{2}k_{F|5i}u_{N,FB|i}}{k_{e,M|12}+k_{e,M|34}+k_{e,F|78}+k_{e,F|56}}=0,
\end{aligned}
\tag{A.48}
$$

while the reaction forces at the crack tip can be expressed as

$$
\begin{cases}
F_{x,CT} & = R_{x,FCT} = \\
& = \left(k_{e,F|77}+k_{e,F|55}\right)u_{x,FCT}+\left(k_{e,F|78}+k_{e,F|56}\right)u_{y,FCT}+\\
& +k_{e,F|75}\cancelto{\approx 0}{u_{x,F}}+k_{e,F|76}\cancelto{\approx 0}{u_{y,F}}+\\
& +\sum_{i=1}^{4}k_{e,F|7i}u_{N,FC|i}+\sum_{i=1,i\neq(5,6)}^{8}k_{e,F|5i}u_{N,FB|i}\\
F_{y,CT} & = R_{y,FCT} = \\
& = \left(k_{e,F|87}+k_{e,F|65}\right)u_{x,FCT}+\left(k_{e,F|88}+k_{e,F|66}\right)u_{y,FCT}+\\
& +k_{e,F|85}\cancelto{\approx 0}{u_{x,F}}+k_{e,F|86}\cancelto{\approx 0}{u_{y,F}}+\\
& +\sum_{i=1}^{4}k_{e,F|8i}u_{N,FC|i}+\sum_{i=1,i\neq(5,6)}^{8}k_{e,F|6i}u_{N,FB|i}
\end{cases}
. \tag{A.49}
$$

Substituting Eq. A.46 in Eq. A.47, Eq. A.48 and Eq. A.49 and solving, we obtain an expression of the form

$$\begin{cases} F_{x,CT} & = K_{xx}u_x + K_{xy}u_y + \\ & + \sum_{i=1}^{4} K_{FC,x|i}u_{N,FC|i} + \sum_{i=1,i\neq(3,4,5,6)}^{8} K_{FB,x|i}u_{N,FB|i} + \\ & + \sum_{i=5}^{8} K_{FC,x|i}u_{N,MC|i} + \sum_{i=7}^{8} K_{MB,x|i}u_{N,FB|i} \\ F_{y,CT} & = K_{yx}u_x + K_{yy}u_y + \\ & + \sum_{i=1}^{4} K_{FC,y|i}u_{N,FC|i} + \sum_{i=1,i\neq(3,4,5,6)}^{8} K_{FB,y|i}u_{N,FB|i} + \\ & + \sum_{i=5}^{8} K_{FC,y|i}u_{N,MC|i} + \sum_{i=7}^{8} K_{MB,y|i}u_{N,FB|i} \end{cases}, \tag{A.50}$$

which can be reformulated synthetically as

$$\begin{cases} F_{x,CT} & = K_{xx}u_x + K_{xy}u_y + \widetilde{F}_x \\ F_{y,CT} & = K_{yx}u_x + K_{yy}u_y + \widetilde{F}_y \end{cases}, \tag{A.51}$$

where $\widetilde{F}_x$ and $\widetilde{F}_y$ represent the influence of the FE solution through the nodes of the elements sharing the crack tip that do not belong to any of the phase interfaces, i.e. the nodes of the elements sharing the crack tip that belong to the bulk of each phase.

B Expression of the VCCT weights matrix for quadrilateral elements with or without singularity

The expression of $\underline{\underline{T}}_{pq}$ for quadrilateral elements with or without singularity is

$$
\underline{\underline{T}}_{pq} = \begin{cases} \underline{\underline{I}} \ for\ p=q<2 \\ \underline{\underline{0}} \ otherwise \end{cases} \quad \text{for } 1^{st} \text{ order quadrilateral elements}
$$

$$
= \begin{cases} \underline{\underline{I}} \ for\ p=q<3 \\ \underline{\underline{0}} \ otherwise \end{cases} \quad \text{for } 2^{nd} \text{ order quadrilateral elements}
$$

$$
= \begin{cases} \underline{\underline{I}} \ for\ p=q<4 \\ \underline{\underline{0}} \ otherwise \end{cases} \quad \text{for } 3^{rd} \text{ order quadrilateral elements}
$$

$$
= \begin{cases} \left(14-\frac{33\pi}{8}\right)\underline{\underline{I}} \ for\ p=1,q=1 \\ \left(-52+\frac{33\pi}{2}\right)\underline{\underline{I}} \ for\ p=1,q=2 \\ \left(17-\frac{21\pi}{4}\right)\underline{\underline{I}} \ for\ p=2,q=1 \\ \left(-\frac{7}{2}+\frac{21\pi}{16}\right)\underline{\underline{I}} \ for\ p=2,q=2 \\ \left(8-\frac{21\pi}{8}\right)\underline{\underline{I}} \ for\ p=1,q=3 \\ \left(-32+\frac{21\pi}{2}\right)\underline{\underline{I}} \ for\ p=2,q=3 \\ \underline{\underline{0}} \ otherwise \end{cases} \quad \text{for } 2^{nd} \text{ order quarter-point quadrilateral elements} \tag{B.52}
$$

$$
= \begin{cases} \left(-11187+\frac{7155\pi}{2}\right)\underline{\underline{I}} \ for\ p=1,q=1 \\ \left(38556-\frac{24543\pi}{2}\right)\underline{\underline{I}} \ for\ p=1,q=2 \\ \left(-53055+\frac{33777\pi}{2}\right)\underline{\underline{I}} \ for\ p=1,q=3 \\ \left(\frac{11396}{3}-\frac{9575\pi}{8}\right)\underline{\underline{I}} \ for\ p=2,q=1 \\ \left(-12936+\frac{33003\pi}{8}\right)\underline{\underline{I}} \ for\ p=2,q=2 \\ \left(17988-\frac{45837\pi}{8}\right)\underline{\underline{I}} \ for\ p=2,q=3 \\ \left(-\frac{8453}{3}+\frac{3595\pi}{4}\right)\underline{\underline{I}} \ for\ p=3,q=1 \\ \left(9804-\frac{12411\pi}{4}\right)\underline{\underline{I}} \ for\ p=3,q=2 \\ \left(-13587+\frac{17289\pi}{4}\right)\underline{\underline{I}} \ for\ p=3,q=3 \\ \left(6948-\frac{17685\pi}{8}\right)\underline{\underline{I}} \ for\ p=1,q=4 \\ \left(-23976+\frac{60993\pi}{8}\right)\underline{\underline{I}} \ for\ p=2,q=4 \\ \left(33372-\frac{84807\pi}{8}\right)\underline{\underline{I}} \ for\ p=3,q=4 \\ \underline{\underline{0}} \ otherwise \end{cases} \quad \text{for } 3^{rd} \text{ order quarter-point quadrilateral elements}
$$

where $\underline{\underline{I}}$ is the identity matrix.

Paper B

Energy release rate of the fiber/matrix interface crack in UD composites under transverse loading: effect of the fiber volume fraction and of the distance to the free surface and to non-adjacent debonds

Authors:
Luca Di Stasio, Janis Varna and Zoubir Ayadi

Reformatted version of paper originally published in:
Theoretical and Applied Fracture Mechanics, Volume 103, October 2019, 102251.

Energy release rate of the fiber/matrix interface crack in UD composites under transverse loading: effect of the fiber volume fraction and of the distance to the free surface and to non-adjacent debonds

Luca Di Stasio[1,2], Janis Varna[2] and Zoubir Ayadi[1]

[1]Université de Lorraine, EEIGM, IJL, 6 Rue Bastien Lepage, F-54010 Nancy, France
[2]Luleå University of Technology, University Campus, SE-97187 Luleå, Sweden

Abstract

The effects of crack shielding, finite thickness of the composite and fiber content on fiber/matrix debond growth in thin unidirectional composites are investigated analyzing Representative Volume Elements (RVEs) of different ordered microstructures. Debond growth is characterized by estimation of the Energy Release Rates (ERRs) in Mode I and Mode II using the Virtual Crack Closure Technique (VCCT) and the J-integral. It is found that increasing fiber content, a larger distance between debonds in the loading direction and the presence of a free surface close to the debond have all a strong enhancing effect on the ERR. The presence of fully bonded fibers in the composite thickness direction has instead a constraining effect, and it is shown to be very localized. An explanation of these observations is proposed based on mechanical considerations.

Keywords: Polymer-matrix Composites (PMCs), Thin-ply, Energy Release Rate, Debonding, Finite Element Analysis (FEA)

A Introduction

Stimulated by the ever more stringent requirements in terms of weight and mechanical performances of the aerospace industry, in recent years the composite community has returned its attention to the mechanisms of intralaminar crack initiation with a focus on thin-ply laminates. Alternative design approaches are now considered based on this non-conventional laminate in applications ranging from cryogenic pressure vessels [23], to airplanes' wings [20], and even reusable space launchers [21].

Thin-ply laminates are the result of a technological innovation, the *spread tow technology*, which consists in opening or spreading the tows, in which fibers (carbon, glass, aramid, basalt among others) are usually shipped in, into very thin tapes used for laminate production. Ply thicknesses of less than 50 μm can nowadays be mass-produced, and record thicknesses of around $20-25$ μm, or $\sim 4-5$ times the average fiber's diameter, have been achieved. In its current form the technique, sometimes referred to as “FUKUI method”, was firstly proposed towards the end of the 1990s [18] and perfected in the subsequent decade [19, 17].

Several experimental investigations on *thin ply* laminates have highlighted their main properties [34, 35, 40, 41, 3, 2, 13]: increased fiber content; more uniform packing of fibers; delay and even suppression of intralaminar cracking (called also transverse-, matrix- or micro-cracking) and delamination. A very insightful work documenting how these phenomena are affected by the morphology of *thin-ply* laminates is the microscopic study of Saito & al. [30], which focuses on the effect of ply thickness on the onset and propagation of intralaminar cracking. In their investigation, tensile tests were performed on carbon fiber/epoxy $[0_2, 90_n, 0_2]$ *thin-ply* laminates for $n = 1, 2, 4$ and the crack density was measured with a digital microscope at several levels of applied tensile strain in the range between 0% and 1.5%. Furthermore, they performed microscopic observations on the specimen's edge at each level of strain. They observed the onset of fiber/matrix interface cracks (referred to as debonds in the following) at lower levels of strain in thinner plies, while at the same time coalescence of debonds and through-the-thickness propagation of transverse cracks in thin plies were delayed and even suppressed as ply thickness decreased. In particular, they reported the first onset of debonds at 0.4% for $n = 1, 2$ and 0.7% for $n = 4$. For $n = 1$, however, at $\varepsilon = 1.5\%$ coalescence of debonds had started to take place but the crack had not completely propagated through the thickness, while for $n = 2$ and $n = 4$ the latter alreay happened at a value of strain respectively of 1.3% and 1%. Our inability to explain these observations with the currently accumulated knowledge demonstrates the necessity of further investigation of interactions between debonds and studies of the constraining (or accelerating) effect of presence of bonded fibers, free and constrained boundaries in the vicinity of a partially debonded fiber.

Early studies on the effect of ply thickness on the onset and propagation of transverse cracks were conducted on glass fiber/epoxy cross-ply laminates by Bailey, Parvizi and collaborators [16, 26, 27], who firstly observed the beneficial effect of thickness reduction on the delay of transverse cracking. They furthermore pointed the attention to the appearance of debonds at the fiber/matrix interface and their subsequent coalescence as the mechanism at the origin of transverse cracks [7]. Moreover, they identified the main mechanical driver of the damage process in the mismatch of elastic properties, and particularly of Poisson's ratios, between fibers and matrix [6]. A full understanding of damage onset and propagation in *thin-ply* laminates thus requires comprehension of the mechanisms governing its very first stage, i.e. the fiber/matrix interface crack. First results were obtained through analytical models in the case of a single fiber with an arc crack (debond) in an infinite matrix under transverse tension by England [14] and Perlman & Sih [28], who obtained the stresses at the interface and calculated the stress intensity factors at the crack tip, and by Toya [36], who evaluated the Energy Release Rate (ERR). Drawing upon the results for the straight bi-material interface crack by Comninou [8], the effect of crack face contact in fiber-matrix debonding was investigated in [24, 37]. In [15], it was showed in terms of ERR why the case of a single asymmetric debond is more likely to be observed under remote transverse tension than two symmetric debonds on the same fiber. The effect of different types and combinations of loads on debonding have been studied for the single fiber model: compression [12], residual thermal stresses [9], and biaxial configurations with different combinations of tension and compression [11, 10]. The effect of the presence of nearby bonded fibers on the debonding of a fiber embedded in an infinite matrix has been studied under uniaxial transverse tension [33], biaxial tension [31] and uniaxial transverse compression [32]. The effect of inter-fiber distance on debond growth has been studied for a partially debonded fiber at the center of a hexagonal cluster inside a homogenized UD composite in the case of fully bonded neighbouring fibers [42] and of two partially debonded fibers out of the surrounding six [39]. An understanding of crack shielding and finite ply thickness effects on debond growth in non-homogenized microstructural models of UDs seems thus to be lacking: this is the problem that we want to address in the present work. Mode I and Mode II energy release rates will be analyzed using stress fields calculated with the FEM for a variety of Repeating Unit Cell (RUC) of the composite with square packing of fibers under transverse tensile loading. The choice of a square packing configuration for the fibers is motivated by its simplicity, as it allows to easily separate the effect of fibers (fully bonded and/or partially debonded) placed along the loading direction from that of fibers placed in the through-the-ply-thickness direction. These RUCs represent composites with different distances between partially debonded fibers and a varying number of bonded fibers between them, which allows to study the effect of crack shielding on the ERR. In the ply thickness direction, the varying number of perfectly bonded fiber rows exposes the effect of the proximity of the free boundary of the composite on debond growth. Finally, using coupling of thickness direction displacements on horizontal boundaries of the RUC, the accelerating effect of the interaction between debonds of fibers located on the same vertical line is studied.

B RVE models & FE discretization

B.1 Introduction & Nomenclature

In this paper, we analyze debond development in unidirectional (UD) composites subjected to in-plane transverse tensile loading. The interaction between debonds in UD composites is studied developing models of different Repeating Unit Cells (RUC) of laminates (see Fig. 1 to Fig. 3) where only the central fiber in the cell has a damage in the form of a fiber/matrix interface crack (debond). The composite RUC may be repeating in the in-plane transverse direction only (representing an ultra-thin composite) or repeating also in the composite thickness direction, representing an infinite composite in a limiting case. Thus, the conditions at the UD composite's upper and lower boundaries are one of the parameters for the investigation. The used RUCs allow for considering the composite with debonds as a sequence of stacked damaged and undamaged fiber rows, each row with only one fiber in the thickness direction. Since all of these RUCs feature regular microstructures with fibers placed according to a square-packing configuration, they are Representative Volume Elements (RVE) of composites with a certain distribution of debonds. Introducing in-plane coordinates x and y, where x is in the transverse direction of the UD composite under consideration, the strain in the y-direction due to a load in the x-direction is small, caused in turn by the very small minor Poisson's ratio of the UD composite. Additionally, debonds are considered to be significantly longer in the fiber direction than in the arc direction. Therefore, we use 2D models under the assumption of plane strain, defined in the $x-z$ section of the composite. Thus, the analysis presented applies to long debonds, with a focus on understanding the mechanisms of growth along their arc direction. The composites are subjected to transverse tensile strain, applied as a constant displacement in the x-direction along the vertical boundary of the RUC as shown in Figures 1 to 4. As the models are differentiated by the number of rows of fibers and by the spacing between debonds along the vertical and horizontal directions, the corresponding RUCs can be distinguished from each other based on the number n of fibers in the horizontal direction and k in the vertical direction. Furthermore, the horizontal surfaces can be either free or vertical displacement coupling can be applied. We thus introduce a common notation $n \times k - free$ and $n \times k - coupling$ to denote a RUC with $n \times k$ fibers and, respectively, a free upper surface or with kinematic coupling applied to it. The specific combinations of particular choices of n, k, and boundary conditions are detailed in Section B.2, together with the description of the corresponding models of damaged composite they are representing.

B.2 Models of Representative Volume Element (RVE)

The first two models feature, as shown in Fig. 1, an ultra-thin UD laminate with only one row of fibers across its thickness, $k = 1$. This is quite an extreme model from the microstructural point of view; however, it allows to focus the analysis on the interaction between debonded fibers placed along the x-direction. Furthermore, as the horizontal surfaces are considered free, the interaction is stronger in this case than in any other, making the trends very clear and the predictions of this model rather conservative. In retrospective, if only 20 years ago such a model would have been considered too abstracted from the physical reality, the recent advancements in the spread tow technology make this approach appealing also as a limiting case for practical considerations.

In the sub-model of Fig. 1a, every n^{th} fiber in the composite is partially debonded on alternating sides of the fiber. The symmetries of the model allow the use of the upper part of the RUC, as highlighted in Fig. 1 to 3. Following the notation introduced in Section B.1, we will refer to this model as $n \times 1 - free$. In the sub-model $n = 1$, Fig. 1b, a debond appears on each fiber on alternating sides and the corresponding RUC contains only one fiber. We will refer to this model as $1 \times 1 - free$.

The second set of models in Fig. 2 and Fig. 3 considers laminates with multiple rows of fibers across the thickness: a finite number of rows in the first two sub-models in Fig. 2; an infinite number in the model of Fig. 3. In Fig. 2a, the RUC contains $n = 1$ fiber in the x-direction, k fibers across the thickness and the central fiber is debonded. This model will be referred to in the following as $1 \times k - free$. Thinking in terms of rows, in this model we have a central row where each fiber is debonded. This row is surrounded

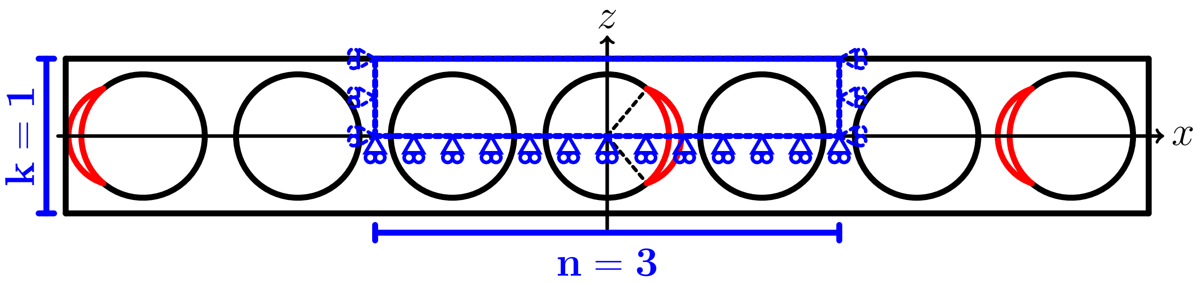

(a) Single row of fibers with a debond appearing every n fibers: model $n \times 1 - free$ ($n = 3$ in the figure).

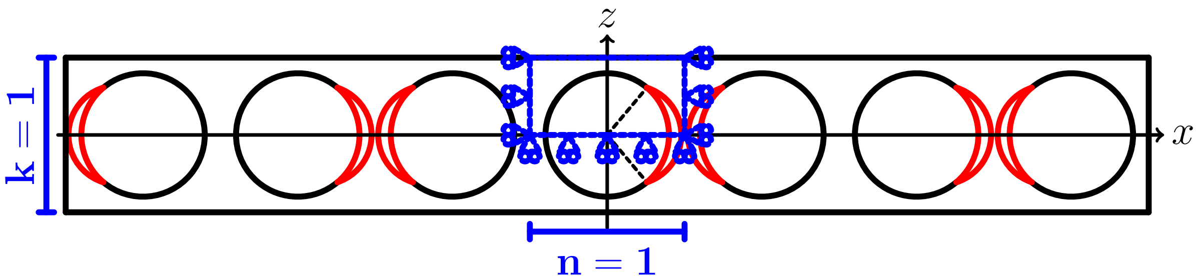

(b) Single row of fibers with debonds appearing on each fiber: model $1 \times 1 - free$.

Figure 1: Models of ultra-thin UD composites with a single "row" of fibers and debonds repeating at different distances.

from each side by $^{(k-1)}/_2$ rows with perfectly bonded fibers. In the sub-model in Fig. 2b, each n^{th} fiber in the central row is debonded and this row is surrounded by $^{(k-1)}/_2$ rows of undamaged fibers from each side. We will refer to this model as $n \times k - free$ (because the horizontal boundary of the RUC is free of any constraint).

Finally, the model in Fig. 3 represents an UD composite with an infinite number of rows; all of them with partially debonded fibers. As all fibers have debonds, the corresponding RUC is made of a single partially debonded fiber with kinematic coupling conditions applied to the upper boundary to assure periodicity. This model is referred to as $1 \times 1 - coupling$.

B.3 Finite Element (FE) discretization

Each RUC is discretized using the Finite Element Method (FEM) within the Abaqus environment, a commercial FEM package [1]. The length l and height h of the model are determined by the number of fibers n in the horizontal direction and k across the thickness (see B.2) according to Eq. B.1:

$$l = 2nL \qquad h = kL; \tag{B.1}$$

where $2L$ is the length of a one-fiber unit, see Fig. 4, defined as a function of the fiber volume fraction V_f and the fiber radius according to

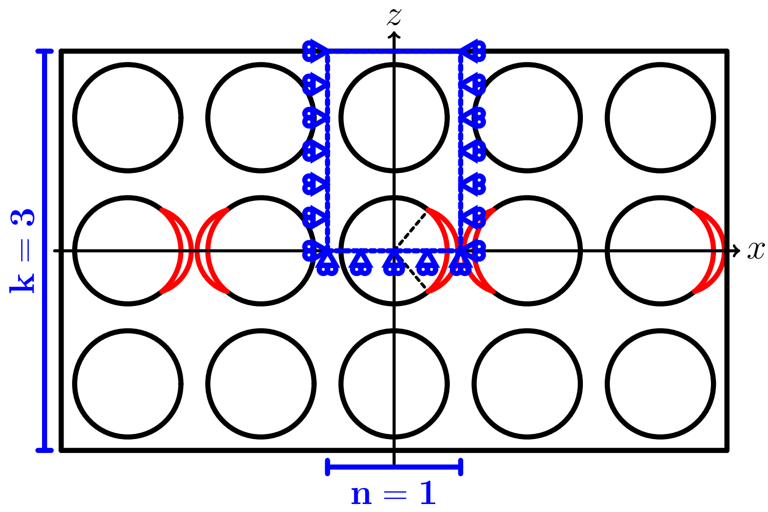

(a) Multiple rows of fibers with debonds appearing on each fiber beloging to the central row: model $1 \times k - free$ ($k = 3$ in the figure).

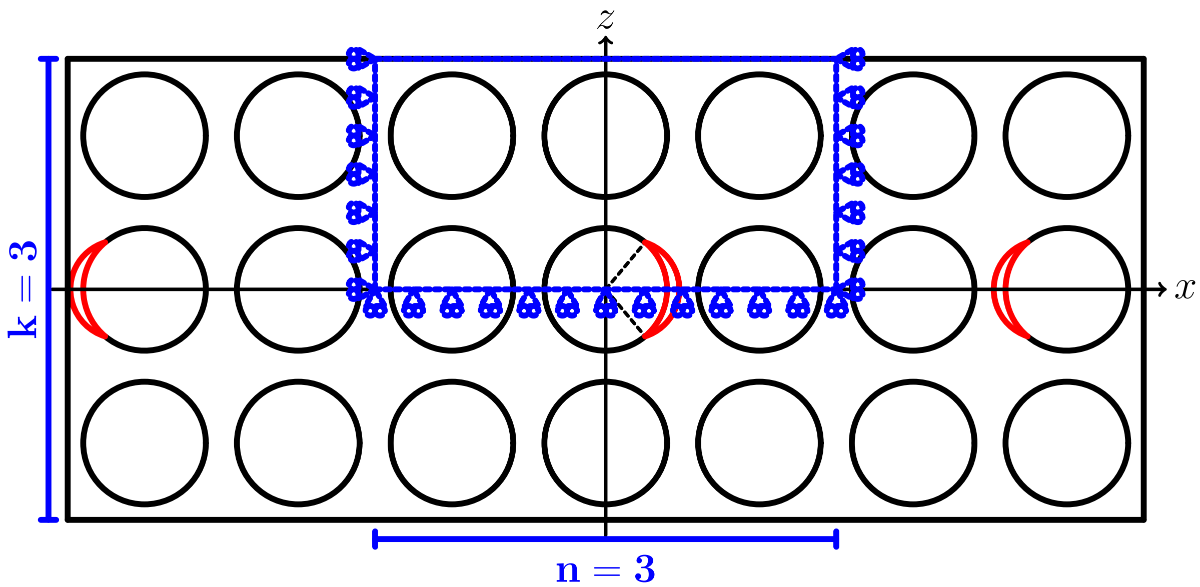

(b) Mutiple rows of fibers with a debond appearing every n fibers within the central row: model $n \times k - free$ ($n = 3$ and $k = 3$ in the figure).

Figure 2: Models of UD composites with different "rows" of fibers and debonds repeating at different distances.

$$L = \frac{R_f}{2}\sqrt{\frac{\pi}{V_f}}. \tag{B.2}$$

The fiber radius R_f is assumed to be the same for each fiber in the model and equal to 1 μm. The latter value is not physical and it has been chosen for simplicity. It is worth to note at this point that, in a linear elastic solution as the one presented here,

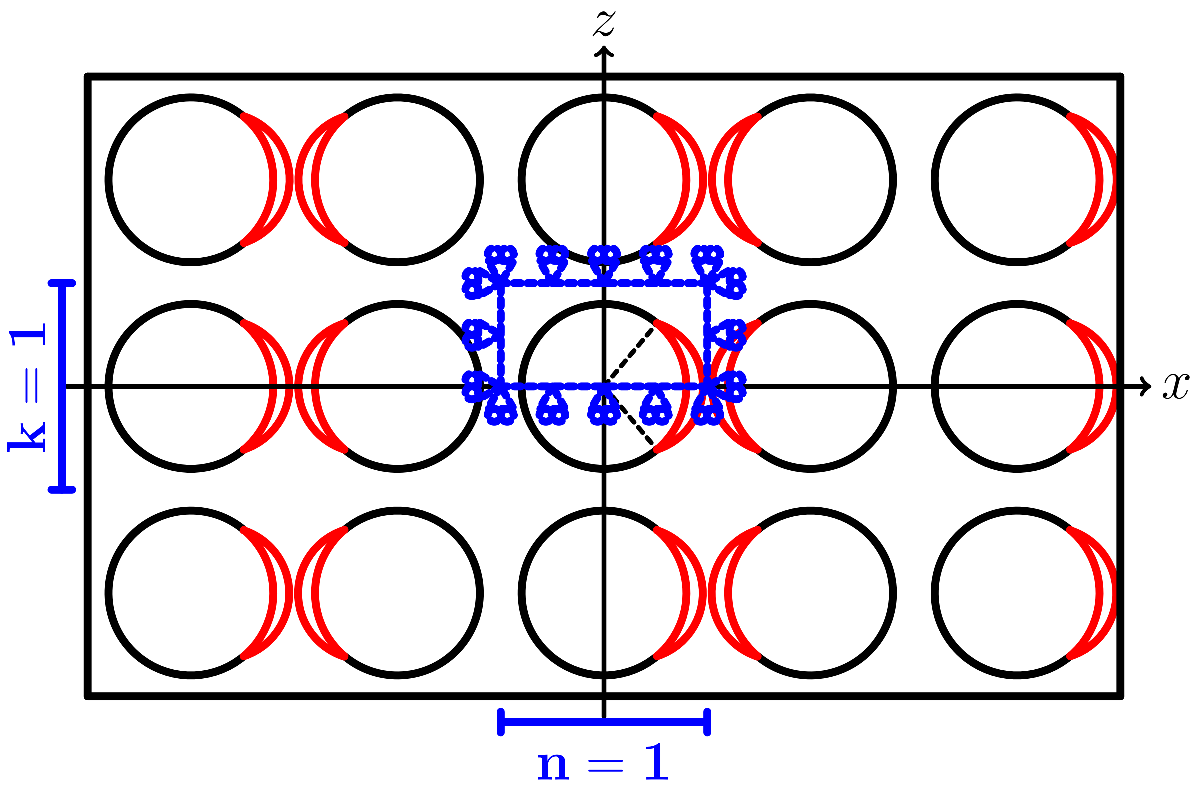

Figure 3: Model of UD composites with an infinite number of "rows" of fibers and debonds appearing on each fiber: model $1 \times 1 -$ *coupling .*

the ERR is proportional to the geometrical dimensions and recalculation of the ERR for fibers of any size, thus, requires a simple multiplication. Furthermore, notice that the relationships in Eqs. B.1 and B.2 ensure that the local and global V_f are everywhere equal.

The debond is placed symmetrically with respect to the x axis (see Fig. 4) and we characterize it with an angular size of $\Delta\theta$ (the full debond size is thus $2\Delta\theta$). For large debond sizes ($\geq 60^\circ - 80^\circ$), a region of variable size $\Delta\Phi$ appears at the crack tip in which the crack faces are in contact and slide on each other. Due to its appearance, frictionless contact is considered between the two crack faces to allow free sliding and avoid interpenetration. The presence of friction at the interface is considered in [38], where the authors model the contact interaction between crack faces using Coulomb's friction with a coefficient $\mu = 0.25$ and show that, for a debond with $\Delta\theta = 80^\circ$, the crack sliding displacement is always different from zero in every point of the crack and only slightly lower than that of the frictionless case. This in turn means that the estimation of G_{II} in the case of frictionless contact provide an upper bound and thus the results presented here represent a conservative estimation (a higher ERR corresponds to higher likelihood of crack propagation). Symmetry with respect to the x axis is applied on the lower boundary. The upper boundary is in general free, except for the model $1 \times 1 -$ *coupling* (Fig. 3) which requires kinematic coupling of vertical displacements also on

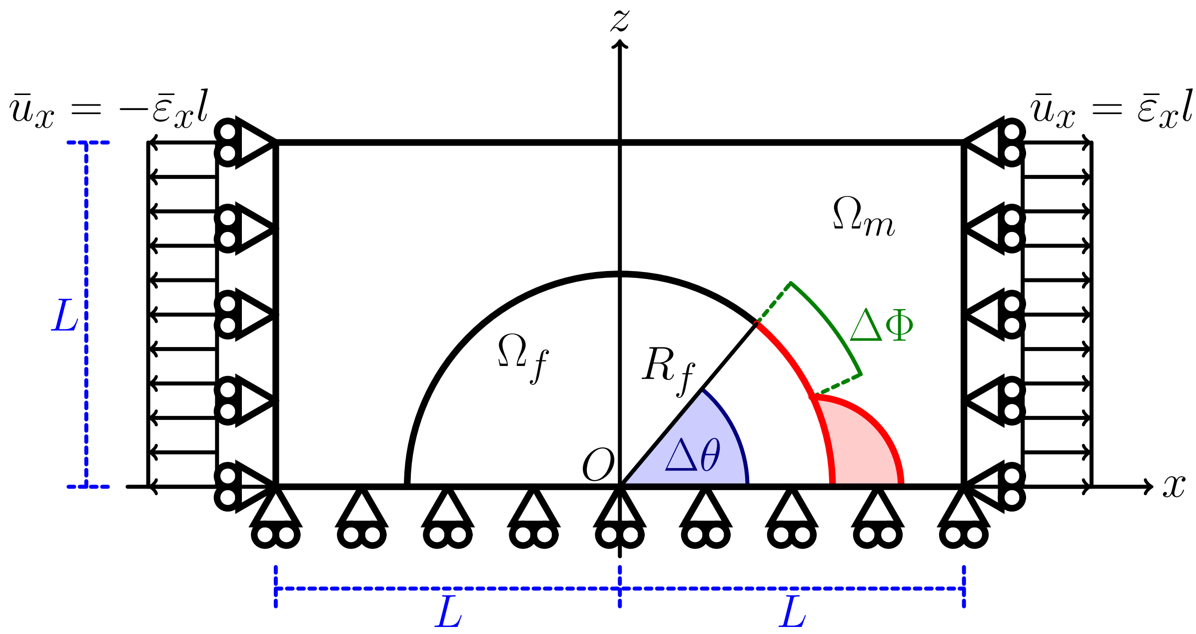

Figure 4: Schematic of the model with its main parameters.

the upper side. Kinematic coupling on the x-displacement is applied along the left and right sides of the model in the form of a constant x-displacement $\pm\bar{\varepsilon}_x l$, corresponding to transverse strain $\bar{\varepsilon}_x$ equal to 1%.

Table 1: Summary of the mechanical properties of fiber and matrix. E stands for Young's modulus, μ for shear modulus and ν for Poisson's ratio.

Material	$E\,[GPa]$	$\mu\,[GPa]$	$\nu\,[-]$
Glass fiber	70.0	29.2	0.2
Epoxy	3.5	1.25	0.4

The model is meshed using second order, 2D, plane strain triangular (CPE6) and rectangular (CPE8) elements, which have respectively 6 and 8 nodes per element. Each node has 2 degrees of freedom, i.e. the horizontal displacement u_x and the vertical displacement u_z. A regular mesh of quadrilateral elements with an almost unitary aspect ratio is required at the crack tip. The angular size δ of an element in the crack tip region is always equal to 0.05°. The overall number of elements needed to discretize the model depends on the debond size $\Delta\theta$ (larger debonds have larger contact zones which require more elements for their correct resolution), the fiber volume fraction (which determines the size of the RVE) and the number of fully bonded fibers present in the model. As an example, the discretization of the $1 \times 1 - free$ model at $V_f = 60\%$ requires a total of 132507 elements for $\Delta\theta = 10°$ and of 296606 elements for $\Delta\theta = 140°$, which corresponds to a minimum required RAM respectively of 445 MB and 1014 MB and to a minimum

RAM needed to minimize I/O operations respectively of 1.63 GB and 3.87 GB. To put it into perspective, the wallclock time required for their solution is respectively 1.3 $[min]$ and 14.95 $[min]$ on a laptop with a 2.5 GHz Intel Core i5 processor and 6 GB of installed RAM. The crack faces are modeled as element-based surfaces and a small-sliding contact pair interaction with no friction is established between them. The Mode I, Mode II and total Energy Release Rates (ERRs) (respectively referred to as G_I, G_{II} and G_{TOT}) represent the main output of the FEM analysis; they are evaluated using the VCCT [22] implemented in a custom Python routine and, for the total ERR, the J-integral [29] is obtained by application of the Abaqus built-in functionality. A glass fiber-epoxy system is considered throughout this paper, and it is assumed that their response lies always in the linear elastic domain. The latter assumption lies on the work of Asp and co-workers, who show that epoxy subjected to a tri-axial stress state as the one observable in the inter-fibers region fails at very low strains ($\sim 0.5\% - 0.8\%$) [5] and in a brittle manner [4], and that the magnitude of deviatoric stresses (evaluated in terms of equivalent Von Mises stress) in the fiber/matrix interface neighborhood does not justify the occurrence of plastic deformations in the case of debond propagation [4]. The properties used are listed in Table 1.

B.4 Validation of the model

The model is validated in Fig. 5 against the results reported in [25, 33], obtained with the Boundary Element Method (BEM) for a single fiber with a symmetric debond placed in an infinite matrix. This situation is modeled using the $1\times 1-free$ RVE with $V_f = 0.0079\%$, which corresponds to a RUC's length and height of respectively $\sim 200R_f$ and $\sim 100R_f$.

To allow for a comparison, the results are normalized following [33] with respect to a reference Energy Release Rate G_0 defined as

$$G_0 = \frac{1+k_m}{8\mu_m}\sigma_0^2\pi R_f \tag{B.3}$$

where μ is the shear modulus, k is the Kolosov's constant defined as $3-4\nu$ for plane strain conditions, R_f is the fiber radius and the index m refers to the properties of the matrix. σ_0 is the stress at the boundary, computed as the average of the stress extracted at each boundary node along the right side (arithmetic average as nodes are equispaced by design along both the left and right sides). The agreement is good: the difference between the BEM solution, which is considered more accurate, and the FEM solution does not exceed 5%. The ERRs' maxima are in the same positions and the size of the contact zone is the same. Nevertheless, an analysis of phenomena leading to less than 5% differences in ERR would not be reliable and, therefore, it is not recommended.

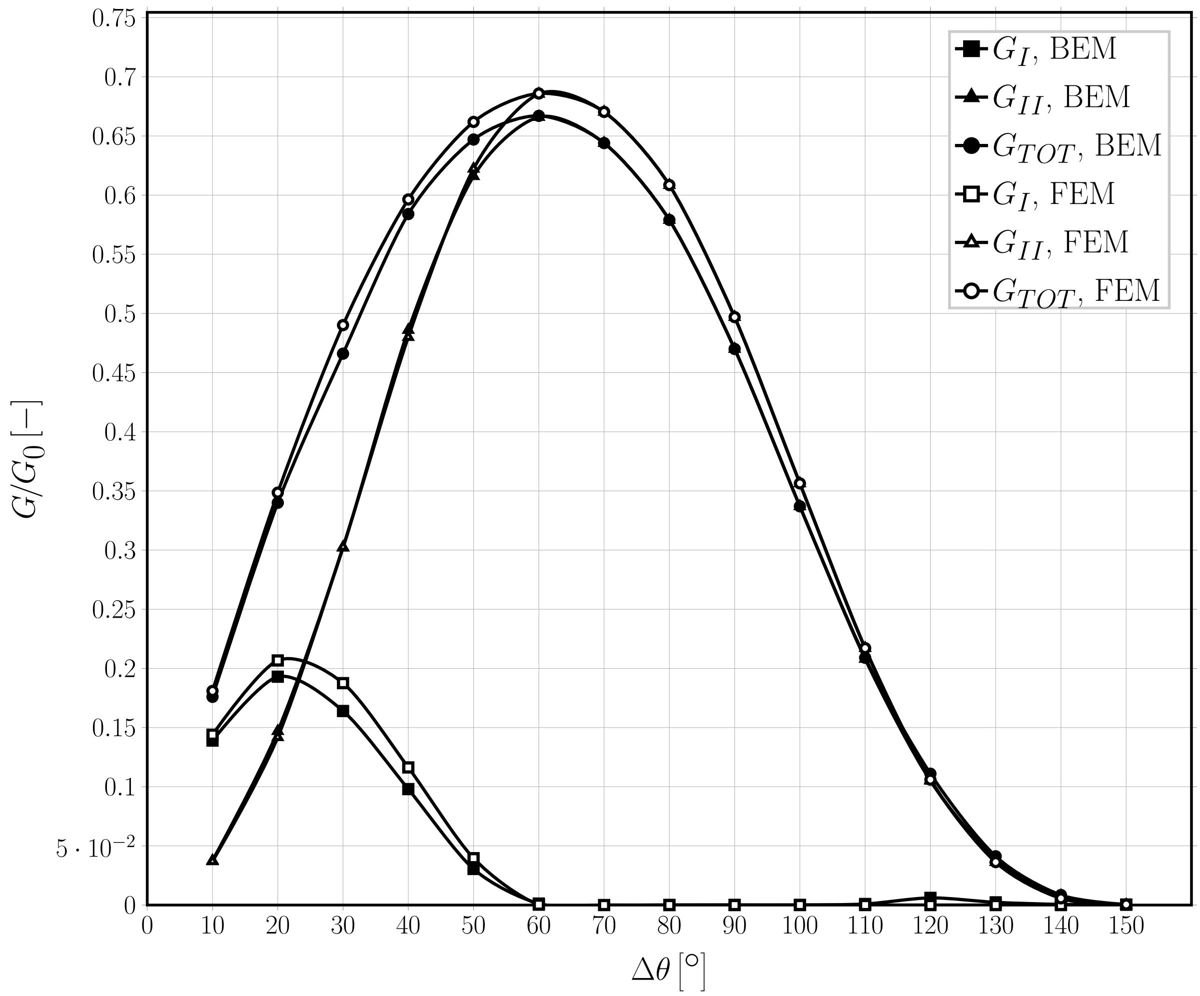

Figure 5: Validation of the single fiber model for the infinite matrix case with respect to the BEM solution in [33].

C Results & Discussion

C.1 Effect of Fiber Volume Fraction

As shown in Figs. 6 and 7, respectively for Mode I and Mode II, the fiber content has a drastic effect on the Energy Release Rate at the tip of the fiber/matrix interface crack. The effect of four levels of fiber volume fraction are compared, 30%, 50%, 60% and 65%, on two microstructural models: a $11 \times 11 - free$ (every 11^{th} fiber in the central fiber row is partially debonded and, on the top of this row, we have 5 undamaged fiber rows), Figs. 6a and 7a, and a $21 \times 21 - free$ (every 21^{th} fiber in the central fiber row is partially debonded and, on the top of this row, we have 10 undamaged fiber rows), Figs. 6b and 7b.

Comparing Fig. 6a with 6b, and Fig. 7a with 7b, we can observe that the ERRs' values are very similar for RUCs with 11×11 and 21×21 fibers, though they are slightly higher for the larger RUC where the next debonded fiber and the free surface are further

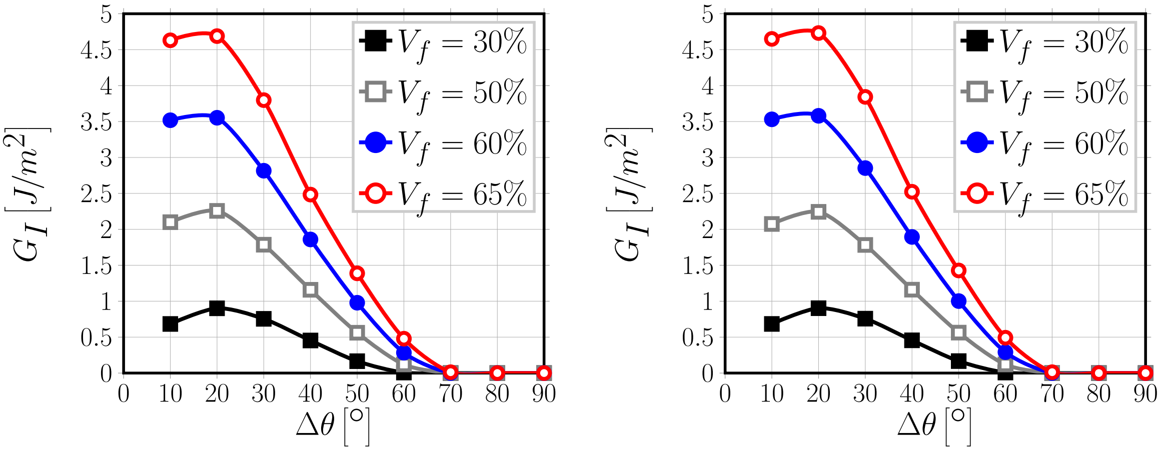

(a) Model $11 \times 11 - free$.

(b) Model $21 \times 21 - free$.

Figure 6: A view of the effect of fiber volume fraction on Mode I ERR in two exemplificative models, subject to an applied transverse strain ε_x of 1%.

away from the debonded fiber. From these results we conclude that both RUCs are large enough to represent a single debonded fiber in an infinite array of bonded fibers. Obviously, there exists a specific effect of the fiber content. For Mode I, Fig. 6, the maximum value of the ERR increases by ~ 5.2 times when V_f changes from 30% to 65%. The debond's angular size for which the peak value occurs remains unchanged at 20°, but for $V_f = 60\%$ and 65% the values of Mode I ERR are rather similar when measured at 10° and at 20°, approximately creating a plateau. Furthermore, increasing the fiber volume fraction delays the onset of the contact zone, which corresponds in Fig. 6 to the first value of $\Delta\theta$ for which G_I is equal to zero. For $V_f = 30\%$, the contact zone first appears for a debond of 60°, similarly to what happens in the single fiber in infinite matrix model (Fig. 5). For higher fiber contents, the contact zone's onset is delayed to a debond's size approximately equal to 70°.

For Mode II, Fig. 7, there is a distinct maximum in the curve and its shape does not depend on the fiber content. The maximum value of the ERR increases by ~ 2.1 times when V_f changes from 30% to 65%. The effect is thus similar to Mode I, but with a significantly lower magnitude. Similar to Mode I, the debond's size for which the peak value of Mode II occurs remains unchanged, at 60°. It is worthwhile to notice that the ratio of Mode II to Mode I peak values is $\frac{max(G_{II})}{max(G_I)} \sim \frac{2.2}{0.9} \sim 2.4$ for $V_f = 30\%$, while it is $\sim \frac{4.7}{4.7} \sim 1$ for $V_f = 65\%$.
The general increasing trends observed in Figs. 6 and 7 are related to the fact that, given that the global and local V_f are everywhere identical in the models presented, an increase in fiber content corresponds to a decrease in the average distance between fibers. Thus, the distances for the decay of the local stress and strain fields in the matrix domain become shorter, leading to higher stresses in general and causing higher values at the crack tip. The difference in relative magnitude between Mode I and Mode II and the delay in the contact zone's onset are instead due to the interplay between two different

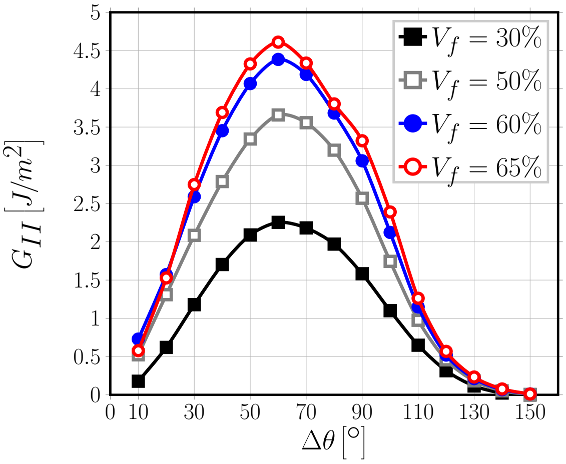

(a) Model $11 \times 11 - free$.

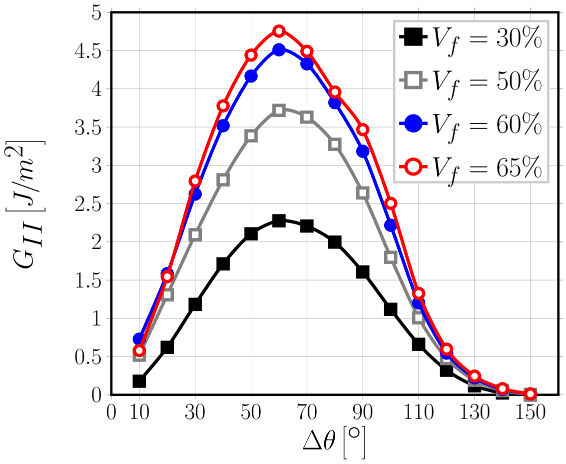

(b) Model $21 \times 21 - free$.

Figure 7: A view of the effect of fiber volume fraction on Mode II ERR in two exemplificative models, subject to an applied transverse strain ε_x of 1%.

mechanisms, both caused by the ordered microstructural arrangement of the model. In the models considered, a fully bonded fiber is always placed along the horizontal direction, aligned with the partially debonded fiber and exactly in front of the debond. By increasing V_f, the former moves closer to the latter and for small debonds this causes a magnification of the x-strain at the crack tip. For small debonds ($\leq 20° - 30°$) in fact, the crack tip is approximately normal to the x-direction and thus an increase in ε_x causes an increase in G_I. On the other hand, for large debonds ($\geq 70° - 80°$) the crack growth direction is almost aligned with the x-axis, thus a magnification in the x-strain translates into an increase of Mode II ERR. However, this increasing effect on G_{II} is partially counteracted by the presence of a fully bonded fiber on top of the debonded fiber and aligned with it. As fibers are more rigid than the surrounding matrix, the presence of the former will restrain horizontal displacements, thus hampering strong increases in G_{II} for large debonds. Furthermore, due to the mismatch in the Poisson's ratios, the fully bonded fiber placed above generates an upward-directed component of the vertical displacement field in the matrix, which tends to open the debond and causes the delay in the contact zone's onset. The interplay between these mechanisms is governed by the average inter-fiber distance and, in turn, by the fiber volume fraction.

These observations are in agreement with the results reported in [33], where the effect on the ERR of a partially debonded fiber of two fully bonded nearby fibers, placed symmetrically with respect to the loading direction, is studied for different angular positions (denoted as θ_2) and radial distances in a model with an effectively infinite matrix ($V_f \sim 0.09\%$). The effect of the former is studied for a constant value of the radial distance between the debonded and bonded fibers, which corresponds to a local V_f^{local} of $\sim 62\%$ assuming hexagonal packing. They report an increase in both Mode I and Mode II ERR with respect to the single fiber case when the two fibers are placed at an angle of respectively $\pm 25°, \pm 30°, \pm 140°, \pm 150°, \pm 155°$, i.e. closest to the loading direction. No-

tice that for $\pm 25°$ and $\pm 155°$ the two fully bonded fibers are almost in contact, with an inter-fiber distance of ~ 0.04 times their radius. This result confirms the considerations made in the previous paragraph about the x-strain magnification caused by the presence of fully bonded fibers along the loading direction. The effect is further analyzed and discussed in Sec. C.2 and Sec. C.4. In the range $\pm 40° - \pm 130°$ instead, the presence of the other fibers causes a reduction of the ERR and, particularly in the range $80° - 120°$, results are very close and almost insensitive to variations in θ_2, which supports the previous conclusion about the effect of a fully bonded fiber on top the partially debonded one. This effect is treated in more detail in Sec. C.3.
Comparing the results from [33] with those presented in this paper, an hypothesis can be furthermore formulated about the robustness of the results of the present article with respect to deviations in fiber position: it seems reasonable to assume a tolerance to deviations of max. $\pm 30°$ with respect to the loading direction and of max. $\pm 20°$ with respect to the through-the-thickness direction.
The effect of the local fiber content is also investigated in [33], by changing the radial distance between the partially debonded fiber and the fully bonded ones. They observe that the further the fully bonded fibers are placed from the central one, i.e. the lower the local V_f, the lower is their effect on the ERR. The magnitude of the effect is however small: the maximum increase of the total ERR is of ~ 1.15 times for $\theta_2 = 30°$ and $150°$ when increasing V_f^{local} from 28% to 62%; the total ERR decreases by a factor of ~ 0.62 for $\theta_2 = 60°$, ~ 0.74 for $\theta_2 = 90°$ and ~ 0.5 for $\theta_2 = 120°$ when increasing V_f^{local} from 28% to 62%. Analogous results can be found in [42], where the authors consider a centrally-placed partially debonded fiber sorrounded by an hexagonal cluster inside an homogenized UD composite. They observe a reduction in the ERR when the local fiber volume fraction is increased, i.e. when the spacing between fibers is reduced. The strongest change is reported for Mode II, which decreases by a factor of ~ 0.73 when the local fiber volume fraction is decreased from 66% to 78%. Thus, the trends presented in [33, 42] are in agreement with our results on the effect of V_f and support the considerations made so far. The stark difference in magnitude however highlights the contrast between the effect of the local fiber volume fraction of a cluster of fibers inside an infinite medium and of the global V_f of long-range microstructural arrangements, such the ones considered in this article. The similarity in trends with the concurrent difference in magnitudes can be explained in relation to the characteristics of the elastic solution computed. In the first case the local fiber volume fraction controls the distance, with respect to the central partially debonded fiber, at which a localized perturbation zone appears in the far-field elastic solution; in the second case the global V_f determines the characteristic lengths of a global periodic solution.

C.2 Interaction between debonds in UD composites with a single row of fibers

The interaction of debonds appearing at regular intervals in an ultra-thin UD composite with a single row of fibers is studied for Mode I (Fig. 8) and Mode II (Fig. 9) and fiber

content equal to 30% (Figs. 8a and 9a) and 60% (Figs. 8b and 9b). The models treated are $3\times1-free$, $5\times1-free$, $7\times1-free$, $11\times1-free$, $21\times1-free$, $101\times1-free$ and $201\times1-free$, corresponding respectively to a debond every 3^{rd}, 5^{th}, 7^{th}, 11^{th}, 21^{st}, 101^{st} and 201^{st} fiber (Fig. 1a). Given that the upper surface of the UD row is left free, the interaction with the debonded fiber in the next RUC is stronger than in any other case and the results of this section are thus the most conservative in terms of debond's growth: the ERRs should be the largest. The effect is enhanced in composites with high V_f and especially for G_{II}: at $V_f = 60\%$ the highest G_{II} value for the $201\times1-free$ composite in Fig. 9b is more than 3 times higher than the G_{II} value value for the $21\times21-free$ composite in Fig. 7b. Even the maximum is shifted to larger angles. The G_I value is for some cases only 30% higher.
From both Fig. 8 and Fig. 9, it can be seen that the presence of a debond close to the analyzed debond decreases the strain magnification effect discussed in Sec. C.1 and thus reduces the value of the ERR. This phenomenon is called "crack shielding" [15].

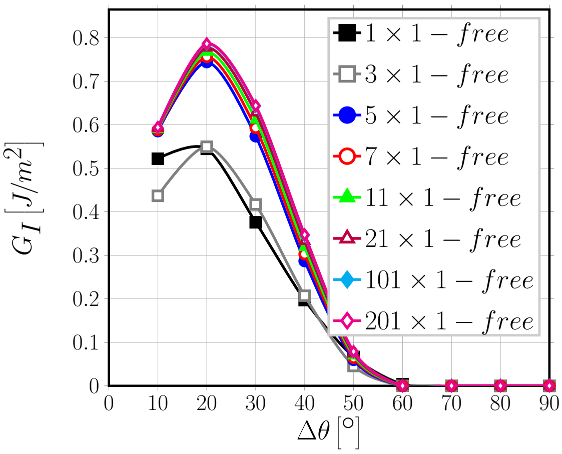

(a) $V_f = 30\%$.

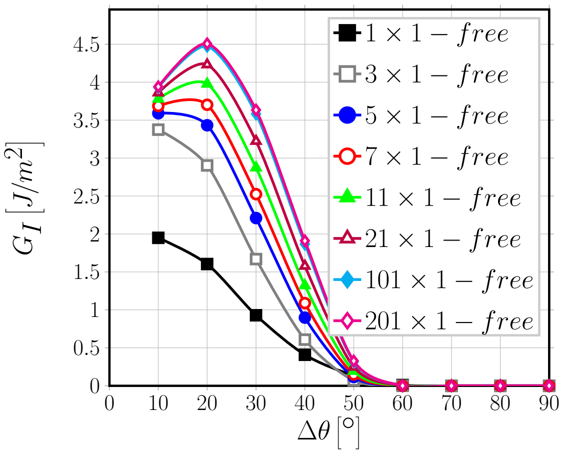

(b) $V_f = 60\%$.

Figure 8: Effect of the interaction between debonds appearing at regular intervals on Mode I ERR in an UD with a single row of fibers at different levels of fiber volume fraction V_f, subject to an applied transverse strain ε_x of 1%.

For Mode I, the presence of a free surface, and inversely the absence of a fully bonded fiber along the vertical direction, implies the absence of the counteracting upward-oriented vertical component of the displacement field due to the mismatch in Poisson's ratios. This in turn translates into the constancy of the value of $\Delta\theta$ corresponding to contact zone's onset, always equal to 60°. For $V_f = 30\%$, Mode I is reduced when the spacing between debonds (in terms of number of fully bonded fibers between them in our models) decreases, but the magnitude of change is significant only in the range when the spacing is reduced from a debond every 5^{th} fiber to one every 3^{rd}. For comparison, the difference of peak G_I values for $V_f = 30\%$ between $5\times1-free$ and $3\times1-free$ is $\sim 0.2\ \frac{J}{m^2}$ (around

30% of the lower value), while between $201 \times 1 - free$ and $5 \times 1 - free$ is $\sim 0.05\ \frac{J}{m^2}$ (around 7% of the lower value). A similar observation can be made for $V_f = 60\%$, but for larger spacings: no difference can be seen between the case of a debond placed every 101^{st} and every 201^{st} fiber. These observations suggest the existence of characteristic distance dependent on the fiber volume fraction which governs the interaction between debonds: in low V_f composites ($V_f = 30\%$) the convergence to a non-interactive solution is faster (less interaction between debonded fibers in neighboring RUCs).

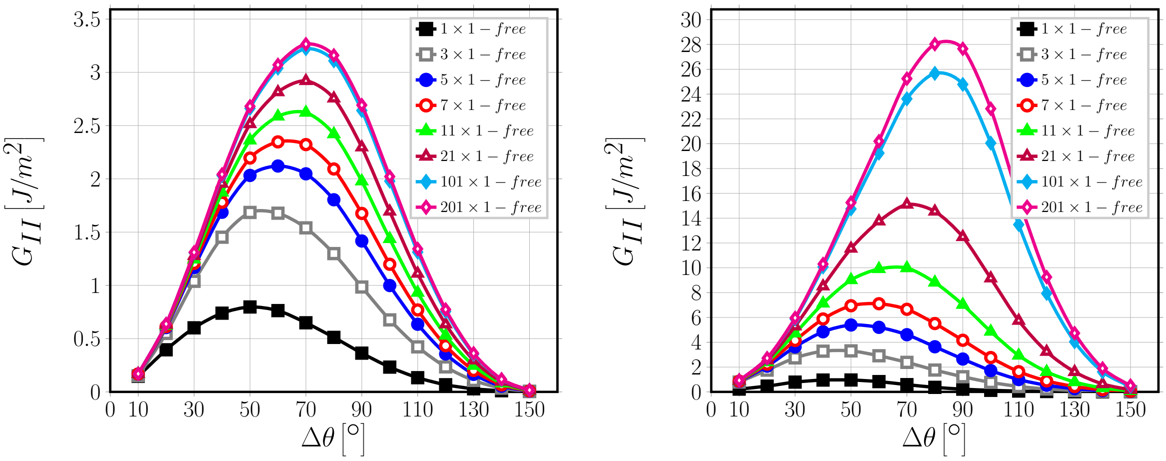

(a) $V_f = 30\%$. (b) $V_f = 60\%$.

Figure 9: Effect of the interaction between debonds appearing at regular intervals on Mode II ERR in an UD with a single row of fibers at different levels of fiber volume fraction V_f, subject to an applied transverse strain ε_x of 1%.

Without costraint on the upper surface, the strain magnification effect creates a larger displacement gap in the x-direction, which increases Mode II for larger debonds. When debonds are far apart, the series of rigid elements in the ultra-thin composite row (constituted by fully bonded fibers and their surrounding matrix) creates higher x-strains than in average in the element with the debonded fiber, which in turn generates higher tangential displacements at the crack tip for larger debonds. Conversely, when debonds are closer (smaller number of rigid elements between them), the strain concentration in the debonded element is more similar to the applied strain (the magnification is reduced) and the tangential displacement component at the crack tip decreases for large $\Delta\theta$. This is the mechanism behind the change in the value of $\Delta\theta$ for which the peak of G_{II} occurs: from 70° to 50° at 30%, and from 80° to 40° at 60% going from the higher to the smaller spacing of debonds. Differently from Mode I, the presence of a characteristic distance is harder to establish. For $V_f = 30\%$ (Fig. 9a), it seems reasonable to establish it at around 100 fully bonded fibers between each debond. For $V_f = 60\%$ (Fig. 9b), the difference between models $101 \times 1 - free$ and $201 \times 1 - free$ is still sizable, thus preventing the establishment of such characteristic distance. It is possible to observe, however, that the change between $101 \times 1 - free$ and $201 \times 1 - free$ is significantly smaller than between $21 \times 1 - free$ and $101 \times 1 - free$ ($2\left[\frac{J}{m^2}\right]$ vs $11\left[\frac{J}{m^2}\right]$), thus suggesting the existence of the characteristic distance outside the range studied. Nevertheless, one should question whether the single row composite with free surface is an appropriate RUC for defining the upper bound for G_{II}: G_{II} may be more affected by the free surface than by the effect of the interaction between debonds in the row.

C.3 Influence of rows of fully bonded fibers on debond's ERR in the middle row

The effect of the presence of rows of fully bonded fibers on debond's growth in the central row with all fibers partially debonded is studied for Mode I (Fig. 10) and Mode II (Fig. 11) and fiber content equal to 30% (Figs. 10a and 11a) and 60% (Figs. 10b and 11b). The models treated are $1 \times 3 - free$, $1 \times 5 - free$, $1 \times 7 - free$, $1 \times 11 - free$, $1 \times 21 - free$, $1 \times 101 - free$ and $1 \times 201 - free$, corresponding to a UD composite with respectively 3, 5, 7, 11, 21, 101 and 201 rows of fibers (Fig. 2a).

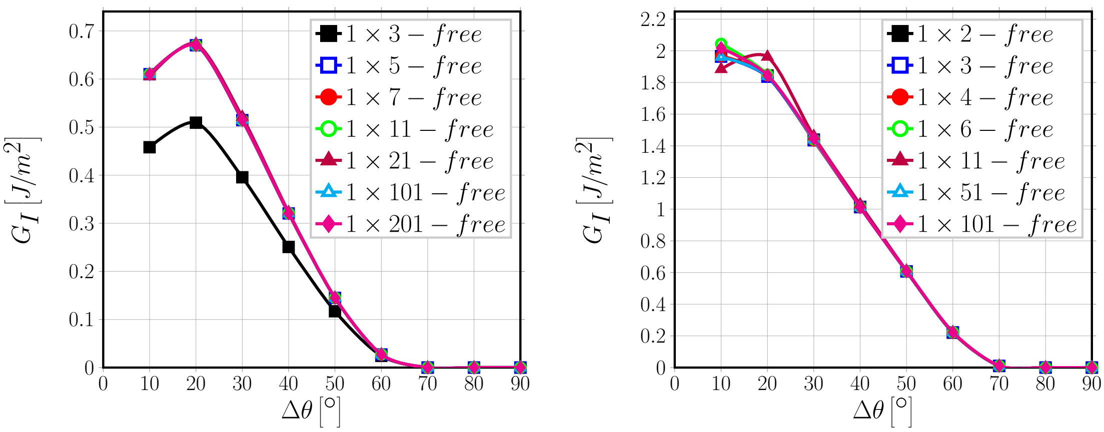

(a) $V_f = 30\%$. (b) $V_f = 60\%$.

Figure 10: Influence of rows of fully bonded fibers on debond's growth in Mode I ERR in a centrally located row of debonded fibers at different levels of fiber volume fraction V_f, subject to an applied transverse strain ε_x of 1%.

The results shown strengthen the arguments made in Sec. C.1 and Sec. C.2. It can, in fact, be seen in Fig. 10 that an increasing number of bonded fiber rows across the thickness delays the onset of the contact zone to a debond of 70° in size, due to the introduction of an additional positive component of the vertical displacement which translates into an opening displacement at the debond's tip.
Comparing Fig. 9b with Fig. 11b, we observe that the presence of bonded fiber rows significantly reduce the G_{II} and its maximum is shifted back to 60°, thus confirming the hypothesis in Section C.2 that the absence of G_{II} convergence with the increasing distance

in a single-row composite is caused more by the free surface than by the interaction between debonds.

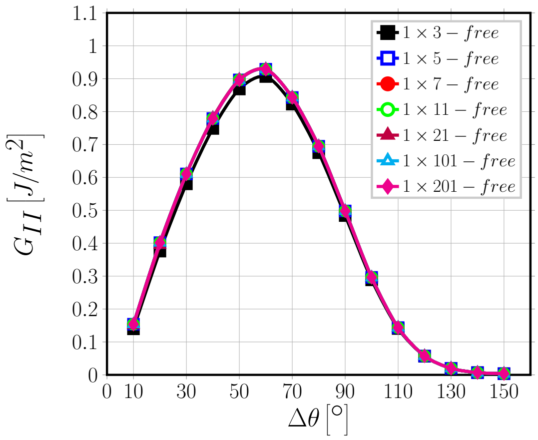

(a) $V_f = 30\%$.

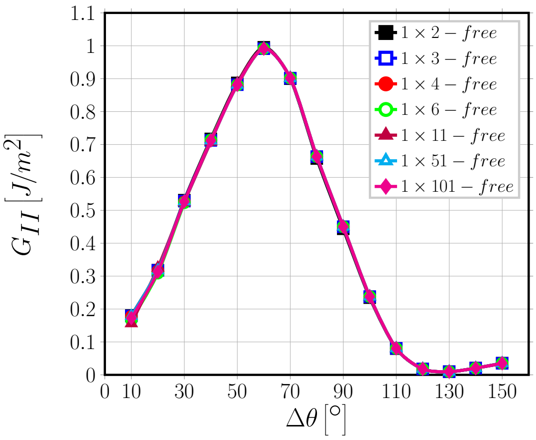

(b) $V_f = 60\%$.

Figure 11: Influence of rows of fully bonded fibers on debond's growth in Mode II ERR in a centrally located row of debonded fibers at different levels of fiber volume fraction V_f, subject to an applied transverse strain ε_x of 1%.

The results of both Mode I and Mode II show that the introduction of an increasing number of fully bonded fiber rows doesn't change the ERR calculated at the crack tip after adding more than one row (the convergence is very fast). A small effect, mostly on Mode I, of the number of bonded fiber rows can be observed at low fiber content (Figs. 10a and 11a), while for high fiber content the smaller model with only one fiber row above the partially debonded one is already representative.

C.4 Effect of multiple rows of bonded fibers on debonding in the central row of a UD composite with different distances between debonded fibers

The ERR of debonds appearing at regular intervals in the central row of fibers in UD composites is affected by the number of rows with bonded fibers. The effect is investigated using different combinations of horizontal debond spacing, controlled by the number of bonded fibers in the central row of the RUC, and the number of rows of bonded fibers on top of it. The following models have been studied: $3\times3-free$, $5\times3-free$, $5\times5-free$, $7\times3-free$, $7\times5-free$, $7\times7-free$, $11\times3-free$, $11\times5-free$, $11\times7-free$, $11\times11-free$, $21\times3-free$, $21\times5-free$, $21\times7-free$, $21\times11-free$, $21\times21-free$, $101\times3-free$, $101\times5-free$, $101\times7-free$, $101\times11-free$, $201\times3-free$, $201\times5-free$, $201\times7-free$, $201\times11-free$ (Fig. 2b).

The results shown in Fig. 12 confirm the observations discussed in Sec. C.2 and

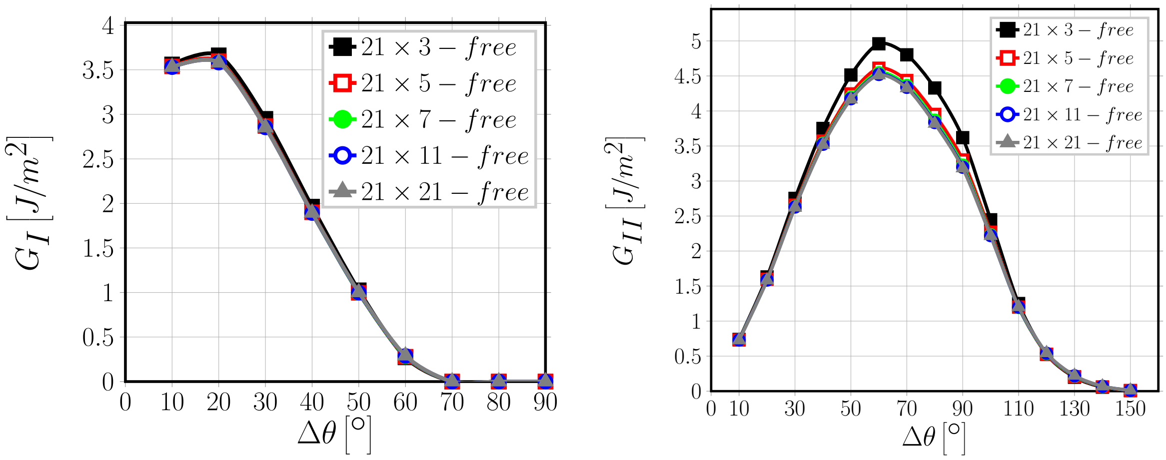

(a) G_I.

(b) G_{II}.

Figure 12: Effect on Mode I and Mode II ERR of the presence of an increasing number of rows of fully bonded fibers in UD composites with debonds appearing every 10^{th} fiber (model $21 \times k - free$). $V_f = 60\%$ and $\varepsilon_x = 1\%$.

Sec. C.3: the presence of fully bonded fiber rows on top of the central row with debonded fibers reduces the interaction with the free surface and thus has a restraining effect on the ERR, that counteracts the magnification due to an increasing number of fully bonded fibers in the horizontal direction. The interplay is further modulated by the fiber content. Observing Fig. 12, it is possibe to note how the free surface interaction decays fast: the presence of 5 fiber rows across the thickness is already sufficient to prevent any significant effect of additional fiber rows on the ERR of a debond in the central row.

The results in Fig. 13 show instead the effect of increasing the distance between two consecutive debonds in the central row of a UD composite of given thickness. In agreement with the observations of Section C.2, increasing the distance between debonds (measured in terms of fully bonded fibers between them) causes an increase in the ERR in both Mode I and Mode II. For both Mode I and Mode II, it is possible to observe the existence of a characteristic distance which defines the limit between the interactive and the non-interactive solution. Furthermore, comparing Figure 13a and 13b, it is possible to notice that Mode I is less sensitive than Mode II to the horizontal spacing of debonds.

C.5 Comparison with the single fiber model with equivalent boundary conditions

The single fiber RUC ($1 \times 1 - free$ or $1 \times 1 - coupling$) corresponds to the most damaged state of the composite, i.e. the state in which all fibers have debonds. The $1 \times 1 - free$ model represents an ultra-thin UD composite with a single row of partially debonded fibers. The $1 \times 1 - coupling$ model, where the displacement coupling is used to enforce periodic boundary conditions, represents an infinite composite.

The comparison of the $1 \times 1 - free$ model with one row multi-fiber models $n \times 1 - free$

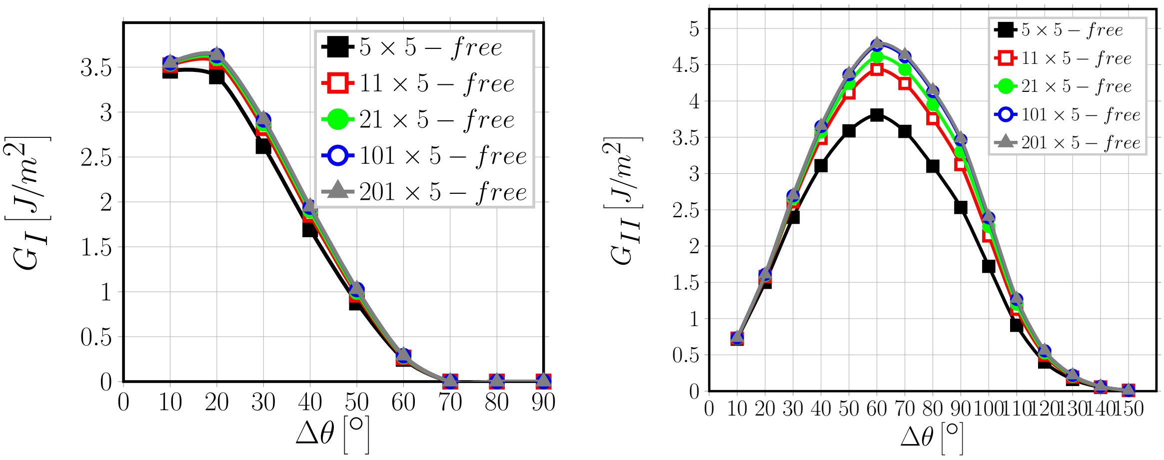

(a) G_I.

(b) G_{II}.

Figure 13: Effect on Mode I and Mode II ERR of increasing the spacing between debonds appearing in the central row of fibers in a UD composite with a fixed number of rows across the thickness. $V_f = 60\%$, $k = 5$ *and* $\varepsilon_x = 1\%$.

in Figure 8 and Figure 9 show that the former provides in general the lowest value of the ERR (the highest crack shielding case).

The $1 \times 1 - coupling$ model is compared with $1 \times 3 - free$ and $1 \times 201 - free$ models in Fig. 14. In all three models the distance between debonds in the x-direction is the same and the difference is in the vertical direction. The $1 \times 1 - coupling$ model describes the interaction between debonds in different rows of debonded fibers whereas the $1 \times k - free$ models describe the effect of the proximity of the composite's free surface. The Mode I ERR in the $1 \times 3 - free$ and $1 \times 201 - free$ model is very similar to the $1 \times 1 - coupling$ model, which leads to a rather surprising conclusion. In both models we have, on the top of the central one, a large amount of fibers (bonded in two cases and debonded in the third case). It appears that the effect of bonded and debonded fibers on the central debond is the same. This implies that, for Mode I ERR, the interaction between debonds in elements placed on top of each other is small.

The same comparison for Mode II shows a sizeable difference in the range $50° - 90°$, while the results almost coincide for smaller values of $\Delta\theta$. The lower values of G_{II} of the $1 \times 1 - coupling$ model in the range $50° - 90°$ are due to the shielding effect of a debond of the same size in the fiber just above the central one (modeled by the coupling boundary condition), which leaves the strip of matrix between the two fibers free to deform away from both of them due to the Poisson's effect and thus favors Mode I and reduces Mode II. This translates into the delay in the appearance of the contact zone, particularly evident in Fig. 14a.

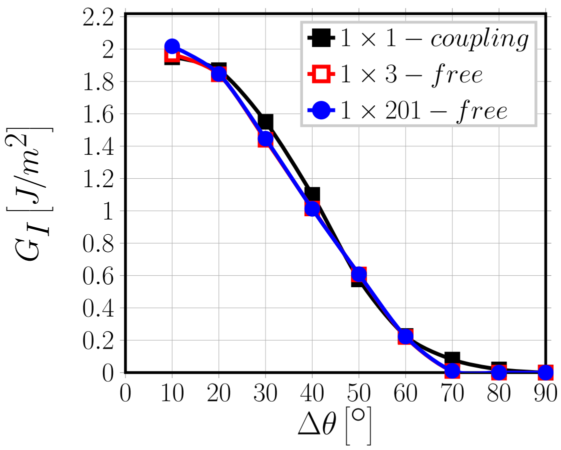

(a) G_I.

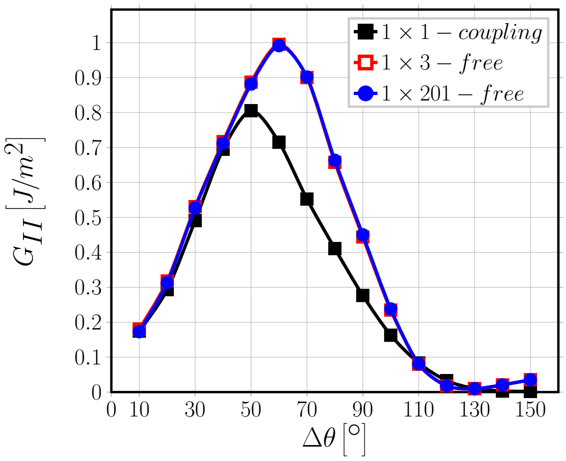

(b) G_{II}.

Figure 14: Comparison of the ERR between the single fiber model with coupling conditions along the upper boundary and the $1 \times k - free$ model. $V_f = 60\%$ and $\varepsilon_x = 1\%$.

D Conclusions & Outlook

Several models of Repeating Unit Cell, representative of different microstructural arrangements of a unidirectional (UD) composite, have been studied in order to investigate the effect on fiber/matrix interface crack growth of the presence of partially debonded and/or fully bonded fibers. Regular microstructures based on square-packing arrangements of fibers have been loaded in transverse tension, with debonds appearing in the central row of fibers at regular intervals measured in terms of number of fully bonded fibers between them. This central row is embedded in-between a varying number of rows with perfectly bonded fibers. The surface of the composite is either traction-free or with imposed vertical displacement constraint imitating a periodic structure in the composite thickness direction.
In each RUC, the fiber volume fraction is spatially homogeneous (no fiber clustering is considered) and the fiber distribution is uniform by design, which establishes a direct relationship between fiber content and inter-fiber distance. The main conclusions of this work are summarized here.

1. With a decreasing number of fully bonded fibers between two partially debonded fibers in the central row, the ERR decreases. It seems to exist a characteristic distance between debonds which defines the transition to a non-interactive solution. However, this distance depends on the number of perfectly bonded fiber rows surrounding the central row and on the fiber volume fraction. This distance can be estimated to be around 100 fully bonded fibers for a 1-fiber-row thick UD with $V_f = 30\%$ and 200 for a 1-fiber-row thick UD with $V_f = 60\%$, while it is expected to be around 100 fibers for a 5-fibers-row thick UD with $V_f = 60\%$.

2. The presence of a free surface close to the debond leads to higher Mode I and Mode

II ERRs and a shift of the peak G values to larger debonds.

3. The presence of fibers (fully or partially bonded) in the composite thickness direction, along the same vertical line as the analyzed central fiber, appears to have a restraining effect on both G_I and G_{II}. The free composite surface effect on the ERR decays very fast: adding more than 2 fully bonded fibers below and above the central row leads to stable constant values of ERR.

4. The presence of a debond in the fiber above the central partially debonded one only delays the appearance of the contact zone, while no significant effect on the ERR has been observed.

5. Increasing the fiber content (decreasing the inter-fiber distance), magnifies in general the effects described in the previous points.

6. The results and conclusions presented agree well with previous observations reported in the literature [33, 42]. A mechanical explanation of the observed trends has been presented based on the mismatch in elastic properties, particularly Poisson's ratios, and the positions of fibers and debonds with respect to the loading direction.

Acknowledgements

Luca Di Stasio gratefully acknowledges the support of the European School of Materials (EUSMAT) through the DocMASE Doctoral Programme and the European Commission through the Erasmus Mundus Programme.

References

[1] *ABAQUS/Standard User's Manual, Version 6.12.* Simulia. Providence, RI, USA, 2012.

[2] R. Amacher et al. "Thin ply composites: Experimental characterization and modeling of size-effects". In: *Composites Science and Technology* 101 (Sept. 2014), pp. 121–132. DOI: 10.1016/j.compscitech.2014.06.027.

[3] A. Arteiro et al. "Large damage capability of non-crimp fabric thin-ply laminates". In: *Composites Part A: Applied Science and Manufacturing* 63 (Aug. 2014), pp. 110–122. DOI: 10.1016/j.compositesa.2014.04.002.

[4] L.E. Asp, L.A. Berglund, and R. Talreja. "A criterion for crack initiation in glassy polymers subjected to a composite-like stress state". In: *Composites Science and Technology* 56.11 (Jan. 1996), pp. 1291–1301. DOI: 10.1016/s0266-3538(96)00090-5.

[5] Leif E. Asp, Lars A. Berglund, and Peter Gudmundson. “Effects of a composite-like stress state on the fracture of epoxies”. In: *Composites Science and Technology* 53.1 (Jan. 1995), pp. 27–37. DOI: 10.1016/0266-3538(94)00075-1.

[6] J. E. Bailey, P. T. Curtis, and A. Parvizi. “On the Transverse Cracking and Longitudinal Splitting Behaviour of Glass and Carbon Fibre Reinforced Epoxy Cross Ply Laminates and the Effect of Poisson and Thermally Generated Strain”. In: *Proceedings of the Royal Society A: Mathematical, Physical and Engineering Sciences* 366.1727 (July 1979), pp. 599–623. DOI: 10.1098/rspa.1979.0071.

[7] J. E. Bailey and A. Parvizi. “On fibre debonding effects and the mechanism of transverse-ply failure in cross-ply laminates of glass fibre/thermoset composites”. In: *Journal of Materials Science* 16.3 (Mar. 1981), pp. 649–659. DOI: 10.1007/bf02402782.

[8] Maria Comninou. “The Interface Crack”. In: *Journal of Applied Mechanics* 44.4 (1977), p. 631. DOI: 10.1115/1.3424148. URL: https://doi.org/10.1115/1.3424148.

[9] E. Correa, V. Mantič, and F. París. “Effect of thermal residual stresses on matrix failure under transverse tension at micromechanical level: A numerical and experimental analysis”. In: *Composites Science and Technology* 71.5 (Mar. 2011), pp. 622–629. DOI: 10.1016/j.compscitech.2010.12.027.

[10] E. Correa, F. París, and V. Mantič. “Effect of a secondary transverse load on the inter-fibre failure under compression”. In: *Composites Part B: Engineering* 65 (Oct. 2014), pp. 57–68. DOI: 10.1016/j.compositesb.2014.01.005.

[11] E. Correa, F. París, and V. Mantič. “Effect of the presence of a secondary transverse load on the inter-fibre failure under tension”. In: *Engineering Fracture Mechanics* 103 (May 2013), pp. 174–189. DOI: 10.1016/j.engfracmech.2013.02.026.

[12] E. Correa et al. “Effects of the presence of compression in transverse cyclic loading on fibre–matrix debonding in unidirectional composite plies”. In: *Composites Part A: Applied Science and Manufacturing* 38.11 (Nov. 2007), pp. 2260–2269. DOI: 10.1016/j.compositesa.2006.11.002.

[13] J. Cugnoni et al. “Towards aerospace grade thin-ply composites: Effect of ply thickness, fibre, matrix and interlayer toughening on strength and damage tolerance”. In: *Composites Science and Technology* 168 (Nov. 2018), pp. 467–477. DOI: 10.1016/j.compscitech.2018.08.037.

[14] A. H. England. “An Arc Crack Around a Circular Elastic Inclusion”. In: *Journal of Applied Mechanics* 33.3 (1966), p. 637. DOI: 10.1115/1.3625132.

[15] I.G. García, V. Mantič, and E. Graciani. “Debonding at the fibre–matrix interface under remote transverse tension. One debond or two symmetric debonds?” In: *European Journal of Mechanics - A/Solids* 53 (Sept. 2015), pp. 75–88. DOI: 10.1016/j.euromechsol.2015.02.007.

[16] K. W. Garrett and J. E. Bailey. "Multiple transverse fracture in 90° cross-ply laminates of a glass fibre-reinforced polyester". In: *Journal of Materials Science* 12.1 (Jan. 1977), pp. 157–168. DOI: 10.1007/bf00738481.

[17] K. Kawabe, H. Sasayama, and S. Tomoda. "New Carbon Fiber Tow-Spread Technology and Applications to Advanced Composite Materials". In: *SAMPE Journal* 45.2 (2008), pp. 6–17.

[18] K. Kawabe, S. Tomoda, and T. Matsuo. "A Pneumatic Process for Spreading Reinforcing Fiber Tow". In: *Proceedings of the* 42nd *International SAMPE Symposium and Exhibition.* (Anaheim, CA, USA). SAMPE, 1997, pp. 65–76.

[19] Kazumasa Kawabe. "New Spreading Technology for Carbon Fiber Tow and Its Application to Composite Materials". Japanese. In: *Sen'i Gakkaishi* 64.8 (2008), pp. 262–267. DOI: 10.2115/fiber.64.p_262.

[20] Yong Han Noel Kim et al. "Effects of Shallow Biangle, Thin-Ply Laminates on Structural Performance of Composite Wings". In: *AIAA Journal* 55.6 (June 2017), pp. 2086–2092. DOI: 10.2514/1.j055465.

[21] Alexander Kopp et al. "The Aurora space launcher concept". In: *CEAS Space Journal* 10.2 (Nov. 2017), pp. 167–187. DOI: 10.1007/s12567-017-0184-2.

[22] Ronald Krueger. "Virtual crack closure technique: History, approach, and applications". In: *Applied Mechanics Reviews* 57.2 (2004), p. 109. DOI: 10.1115/1.1595677.

[23] Douglas A. McCarville et al. "3.5 Design, Manufacture and Test of Cryotank Components". In: *Comprehensive Composite Materials II*. Elsevier, 2018, pp. 153–179. DOI: 10.1016/b978-0-12-803581-8.09958-6.

[24] F. París, J. C. Caño, and J. Varna. "The fiber-matrix interface crack — A numerical analysis using Boundary Elements". In: *International Journal of Fracture* 82.1 (May 1996), pp. 11–29. DOI: 10.1007/bf00017861.

[25] Federico París, Elena Correa, and Vladislav Mantič. "Kinking of Transversal Interface Cracks Between Fiber and Matrix". In: *Journal of Applied Mechanics* 74.4 (2007), p. 703. DOI: 10.1115/1.2711220.

[26] A. Parvizi and J. E. Bailey. "On multiple transverse cracking in glass fibre epoxy cross-ply laminates". In: *Journal of Materials Science* 13.10 (Oct. 1978), pp. 2131–2136. DOI: 10.1007/bf00541666.

[27] A. Parvizi, K. W. Garrett, and J. E. Bailey. "Constrained cracking in glass fibre-reinforced epoxy cross-ply laminates". In: *Journal of Materials Science* 13.1 (Jan. 1978), pp. 195–201. DOI: 10.1007/bf00739291.

[28] A.B. Perlman and G.C. Sih. "Elastostatic problems of curvilinear cracks in bonded dissimilar materials". In: *International Journal of Engineering Science* 5.11 (Nov. 1967), pp. 845–867. DOI: 10.1016/0020-7225(67)90009-2.

[29] J. R. Rice. “A Path Independent Integral and the Approximate Analysis of Strain Concentration by Notches and Cracks”. In: *Journal of Applied Mechanics* 35.2 (1968), p. 379. DOI: 10.1115/1.3601206.

[30] Hiroshi Saito, Hiroki Takeuchi, and Isao Kimpara. “Experimental Evaluation of the Damage Growth Restraining in 90° Layer of Thin-ply CFRP Cross-ply Laminates”. In: *Advanced Composite Materials* 21.1 (2012), pp. 57–66. DOI: 10.1163/156855112X629522.

[31] C. Sandino, E. Correa, and F. París. “Composite materials under transverse biaxial loads: Study of the influence of a nearby fibre on the interface crack growth under tension”. In: *Proceeding of the* 17^{th} *European Conference on Composite Materials (ECCM-17).* (Munich, Germany, June 26–30, 2016). 2016.

[32] C. Sandino, E. Correa, and F. París. “Interface crack growth under transverse compression: nearby fibre effect”. In: *Proceeding of the* 18^{th} *European Conference on Composite Materials (ECCM-18).* (Athens, Greece, June 24–28, 2018). 2018.

[33] C. Sandino, E. Correa, and F. París. “Numerical analysis of the influence of a nearby fibre on the interface crack growth in composites under transverse tensile load”. In: *Engineering Fracture Mechanics* 168 (Dec. 2016), pp. 58–75. DOI: 10.1016/j.engfracmech.2016.01.022.

[34] H. Sasayama et al. “Effect of lamina thickness on first ply failure in multidirectionally laminated composites”. In: *Proceedings of the* 8^{th} *Japan SAMPE Symposium.* (Tokyo, Japan). SAMPE, 2003.

[35] S. Sihn et al. “Experimental studies of thin-ply laminated composites”. In: *Composites Science and Technology* 67.6 (May 2007), pp. 996–1008. DOI: 10.1016/j.compscitech.2006.06.008.

[36] M. Toya. “A crack along the interface of a circular inclusion embedded in an infinite solid”. In: *Journal of the Mechanics and Physics of Solids* 22.5 (Oct. 1974), pp. 325–348. DOI: 10.1016/0022-5096(74)90002-7.

[37] J. Varna, Federico París, and J. C.Caño. “The effect of crack-face contact on fiber/matrix debonding in transverse tensile loading”. In: *Composites Science and Technology* 57.5 (1997), pp. 523–532. DOI: 10.1016/s0266-3538(96)00175-3.

[38] Janis Varna, Federico Paris, and Juan Carlos del Cano. “The effect of crack-face contact on fiber/matrix debonding in transverse tensile loading”. In: *Composites Science and Technology* 57.5 (1997), pp. 523–532. DOI: 10.1016/s0266-3538(96)00175-3.

[39] Janis Varna et al. “Growth and Interaction of Debonds in Local Clusters of Fibers in Unidirectional Composites during Transverse Loading”. In: *Key Engineering Materials* 754 (Sept. 2017), pp. 63–66. DOI: 10.4028/www.scientific.net/kem.754.63.

[40] Tomohiro Yokozeki, Yuichiro Aoki, and Toshio Ogasawara. "Experimental characterization of strength and damage resistance properties of thin-ply carbon fiber/toughened epoxy laminates". In: *Composite Structures* 82.3 (Feb. 2008), pp. 382–389. DOI: 10.1016/j.compstruct.2007.01.015.

[41] Tomohiro Yokozeki et al. "Damage characterization in thin-ply composite laminates under out-of-plane transverse loadings". In: *Composite Structures* 93.1 (Dec. 2010), pp. 49–57. DOI: 10.1016/j.compstruct.2010.06.016.

[42] Linqi Zhuang et al. "Effects of inter-fiber spacing on fiber-matrix debond crack growth in unidirectional composites under transverse loading". In: *Composites Part A: Applied Science and Manufacturing* 109 (June 2018), pp. 463–471. DOI: 10.1016/j.compositesa.2018.03.031.

Paper C

Yet Another Sub-Optimal Estimator of Sinusoids in Noise

Authors:
Dr. C

Reformatted version of paper submitted to:
Example Thesis, Internal Report, Luleå University of Technology, 2009.

Paper D

An example of a yet-to-be-submitted paper

Authors:
Dr. C

To be submitted.